Fall 2015

Fabrication, Characterization, and Application of Carbon Nanoparticles for the Detection of Heavy Metal Ions in Aqueous Media

Aaron Michael Simpson

FABRICATION, CHARACTERIZATION, AND APPLICATION OF CARBON NANOPARTICLES FOR THE DETECTION OF HEAVY METAL IONS IN AQUEOUS MEDIA

A Masters Thesis

Presented to

The Graduate College of

Missouri State University

In Partial Fulfillment

Of the Requirements for the Degree

Master of Science, Chemistry

By

Aaron Michael Simpson

December 2015

FABRICATION, CHARACTERIZATION, AND APPLICATION OF CARBON NANOPARTICLES FOR THE DETECTION OF HEAVY METAL IONS IN AQUEOUS MEDIA

Chemistry

Missouri State University, December 2015

Master of Science

Aaron Michael Simpson

ABSTRACT

This research set out to develop a method for producing Carbon nanoparticles (CNPs) from glycerol and use them to detect Cu^{2+}, Hg^{2+}, and Pb^{2+} ions in aqueous solution. Three synthesis methods were developed using the following mixtures: (1) glycerol and silica, (2) glycerol, silica, and H_3PO_4, and (3) glycerol with H_3PO_4. The structure of the particles was characterized using a variety of spectroscopic techniques. Size distributions were obtained from scanning electron microscopy images. The particles were spherical with average diameters of 66, 58, and 89 nm respectively and believed to consist of a carbon core with carboxylic acid and alcohol functional groups on the surface. Glassy carbon electrodes modified with CNPs were used for metal detection by square wave voltammetry and the following parameter were optimized: electrode preparation, accumulation time, reduction time, reduction potential, pulse height, and pulse width. Calibration curves for each metal were produced and detection limits were calculated. The detection limits for Cu^{2+}, Hg^{2+}, and Pb^{2+} were 0.50 ppm, 31 ppm and 0.30 ppm and the sensitivity of the calibration curves were 13.8 mA/ppm, 0.994 mA/ppm, and 40.4 mA/ppm respectively. These detection limits were compared to the maximum contaminant limits set by the EPA and it was shown that this system could detect Cu^{2+} at levels lower than the set limits.

KEYWORDS: carbon nanoparticles, fluorescence, square wave voltammetry, lead, copper, mercury

This abstract is approved as to form and content

_____

Adam K. Wanekaya, PhD
Chairperson, Advisory Committee
Missouri State University

FABRICATION, CHARACTERIZATION, AND APPLICATION OF CARBON NANOPARTICLES FOR THE DETECTION OF HEAVY METAL IONS IN AQUEOUS MEDIA

By

Aaron Michael Simpson

A Masters Thesis
Submitted to the Graduate College
Of Missouri State University
In Partial Fulfillment of the Requirements
For the Degree of Master of Science, Chemistry

December 2015

Approved:

_____
Adam K. Wanekaya, PhD

_____
Kartik C. Ghosh, PhD

_____
Reza Sedaghat-Herati, PhD

_____
Matthew R. Siebert, PhD

_____
Julie Masterson, PhD: Dean, Graduate College

ACKNOWLEDGEMENTS

I must thank many people who offered advice and support during my graduate studies. Dr. Adam Wanekaya's patience and wisdom is responsible for development as a research scientist. Next, Dr. Nikolay Gerasimchuk and Dr. Reza Herati always welcomed my questions and the use of their equipment. I would also like to acknowledge the patience and guidance offered to me by my Thesis Committee: Dr. Adam Wanekaya, Dr. Kartik Ghosh, Dr. Reza Herati, and Dr. Matthew Siebert. Also, Dr. Ghosh and his graduate students (Mr. Haque and Mr. Mamun) gave considerable help with obtaining the XRD patterns for my materials. I am very appreciative of the high quality laboratory environment provided by my fellow and former research group members: Ramyah Aaryasomayajula, Steven Caudle, Tyler Coonis, Molly Duszynski, Geoffrey Manani, Hillary Warden, and Jam Webber. Partial funding for this research was given by the Missouri State University Chemistry Department and Missouri State University Graduate College. Finally, I must thank my family and friends for their continuous support.

I dedicate this thesis to my parents: Barbara L. Simpson and Jerry D. Simpson.

TABLE OF CONTENTS

LIST OF TABLES

LIST OF FIGURES

CHAPTER 1: INTRODUCTION TO CARBON NANOPARTICLES

1.1.0 Introduction

In recent years the study of materials with dimensions in the nanometer range has exploded. This is primarily due to the characteristics of these materials and how they are different from the characteristics when they have larger dimensions. For example, gold nanoparticles can display a red color when in solution with water, a far cry from the color of gold jewelry we are used to seeing.

One area of research that has found much interest over the past few years is the area of carbon quantum dots (Cdots). Cdots get their name from their size and fluorescence properties. They are nanoparticles believed to have an sp^2-hybridized carbon core with sp^3-hybridized carbons scattered randomly throughout.[1, 2] These sp^3-hybridized carbons are believed to connect or bind the particle together. The proposed structure is similar to graphite, but with sp^3 carbons bonding the layers together. Graphite has layers of sp^2-hybridized carbons arranged in a continuous hexagonal or honeycomb pattern. These layers can be pulled apart and if the number of layers is small enough, then the material is known as graphene. Graphene has several derivatives including Fullerenes and nanotubes. All three fluoresce to some extent, but Cdots have a much higher quantum yield. Another form of carbon is diamond, which has a continuous sp^3-hybridized carbon structure.

Highly fluorescent carbon particles were first discovered in 2004 by Xu et al.[3] They were described as "fluorescent nanotube fragments." Over the years since their

discovery, they have become known as Cdots for particles smaller than ~10 nm and carbon nanoparticles (CNPs) for sizes larger than ~10 nm.

Most quantum dots are made from metal semiconductors, such as cadmium(II) sulfide and are nanoparticles with dimensions close enough to the Bohr exciton radius to results in a quantum confinement effect, which gives a size dependent fluorescence emission spectrum.[4] Therefore, the color of the emitted light may be tuned by controlling the size of the particles accomplished by changing the reaction parameters. Unlike these metal quantum dots, the fluorescence of Cdots is not dependent upon the size of the particles. Zuo et al. have produced CNPs with sizes in the 120 nm range that demonstrate a fluorescence spectrum similar to that of Cdots with sizes around 10 nm.[5]

The fluorescence spectrum of Cdots is also unique among quantum dots in another way. The emission peak is broad spanning from blue to the near infrared when excited with ultraviolet light (see Figure 1). It has a maximum intensity between 450 nm to 550 nm and falls off gradually as you move to longer wavelengths. The wavelength of maximum intensity varies depending on the carbon source used in synthesis and the substance used to passivate the surface. [1, 6] The spectrum can be truncated by increasing the excitation wavelength. This is commonly referred to in the literature as "tuning" the emission.[6-9] This is another place where Cdots differ from metal containing quantum dots. These metal quantum dots emit light at a particular wavelength that is dependent on the size of the particle and generally have a narrow emission peak. This means that changing the excitation wavelength does not affect the observed emission color. This has promise for bioimaging since the emission wavelength can be selected to eliminate cell

intrinsic fluorescence interference. Combining their fluorescence with low cell toxicity, allows for their use in many biological applications. [10, 11, 12]

The consensus in the literature is that the fluorescence spectrum of Cdots is due to defects on the surface of the particles.[1, 13] Since the defects are the same for any size of particle, the fluorescence spectrum is consistent at any particle size. These defects are areas where heteroatoms are bonded to the carbons on the surface of the particles or where the sp^2 carbon continuity is disrupted.[1, 2, 14] This creates "islands" of emitters, and the wide emission spectrum results.[1] Recent studies suggest that the core of the Cdots is responsible for the blue emission, while oxygen containing functional groups on the surface are responsible for the higher wavelength emission.[1, 2, 6, 13] Cdots are not exactly quantum dots in the conventional sense. They seem to be more accurately described as a particle made of many emitters.

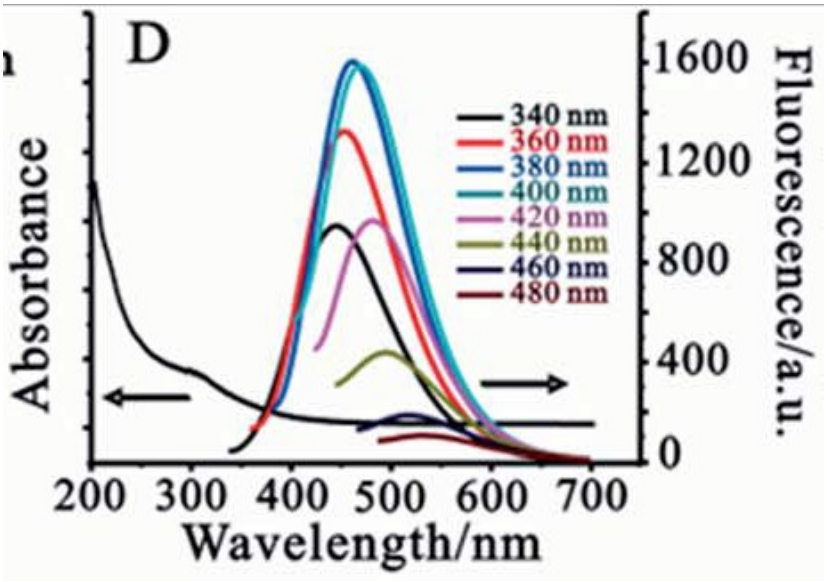

Figure 1: Fluorescence Spectra of CNPs at Different Excitation Wavelengths.[15] As the excitation wavelength is increased, the fluorescence peak shifts to longer wavelengths.

The fact that Cdots emit light over a wide range while metal quantum dots give a narrow range has benefits and drawbacks. For one, any size of Cdot will give a predictable emitting range, which allows for selection of observed fluorescence emission while metal quantum dots must be specifically designed for the desired fluorescence emission. On the other hand, the opposite is also true: if there is a need to excite at a specific wavelength, let us say, in the ultraviolet range and you need the dots to emit in the red region of the visible spectrum, then filters must be used for the Cdots, whereas with the metal quantum dots, no filter is needed if using the correct metal quantum dots. More of the Cdots' properties will be demonstrated in the next section, which gives an overview of their applications from literature.

1.2.0 Current Applications in Literature

The unique properties of Cdots have allowed for a wide range of applications. These applications range from cell imaging to light emitting diodes. [12-13, 16-32] Most of these applications make use of the fluorescence of these materials. In this section, a few representative applications will be highlighted.

One of the most common uses for Cdots has been in cell imaging. [7, 10-12, 15, 33-39] Gong et al. demonstrated recently that Cdots produced from ascorbic acid can be used to image breast cancer cells (Bcap-37) and normal breast tissue cells (Hs-578) with high cell viability of 78% and 88%, respectively.[11] They imaged the cells using a confocal fluorescence microscope and found that the Cdots were taken up by the cells efficiently. The images can be seen in Figure 2, which shows that the Cdots were well dispersed throughout the cell interior.

Specific targeting of cells has also been accomplished with Cdots.[10, 13, 21, 40] An example of this can be demonstrated by the conjugation of Cdots with aptamers. Aptamers are small oligonucleotides with a specific base sequence designed to target certain chemical moieties found in cells. Recently, Cdots were made by microwave pyrolysis of a mixture of glycerol and 2-mercaptoethanol.[41] This formed Cdots with thiol groups on the surface. The researchers then attached TTA1 aptamers via a terminal maleimide-thiol reaction.[41] This aptamer targets tenascin, which is an over expressed protein found on the cell membrane of certain cancer cells.[41] They then incubated three cell lines with these aptamer conjugated Cdots, which were non-cancerous Chinese hamster ovary (CHO), human cervical cancer (HeLa), and rat glioma cancer cells (C6).[41] The results showed that the aptamer-Cdots had a significant selectivity toward the two cancer cell lines (see Figure 3).[41]

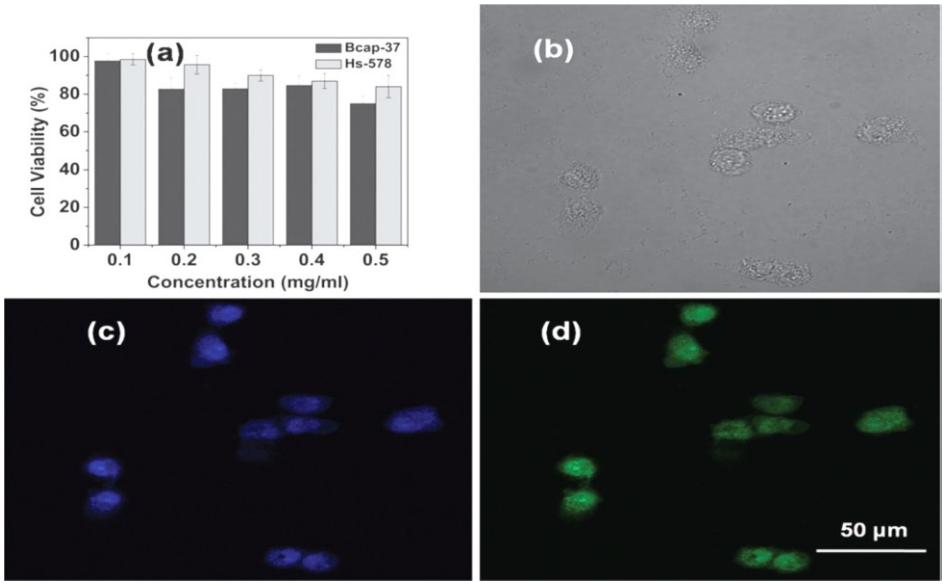

Figure 2: The Use of Cdots to Image Breast Cancer Cells.[11] Cell viability study for the Cdots made from ascorbic acid (a), "brightfield" image the BCap-37 cells incubated with the Cdots (b), and the same area illuminated with 405 nm (c) and 488 nm (d) light as viewed with a confocal microscope.[11]

CNPs have been applied in the photothermal therapy field. [10, 21] Photothermal therapy is a means of destroying cells by heat. The cells take up a material, chemical, or particles that can absorb near-infrared light and convert it to heat.[10, 21] This heat then destroys the cells. Tu et al. produced CNPs from activated carbon and passivated the surface with polyethylene glycol (PEG).[10] These PEGylated CNPs showed little fluorescence, which was believed to increase their usefulness in photothermal therapy.[10] Upon incubation of MCF-7 human breast cancer cells for 24 hours in the PEGylated CNPs and subsequent irradiation with a 808 nm laser for 5 min, the viability of the cells dropped by nearly 75% (see Figure 4).[10, 42]

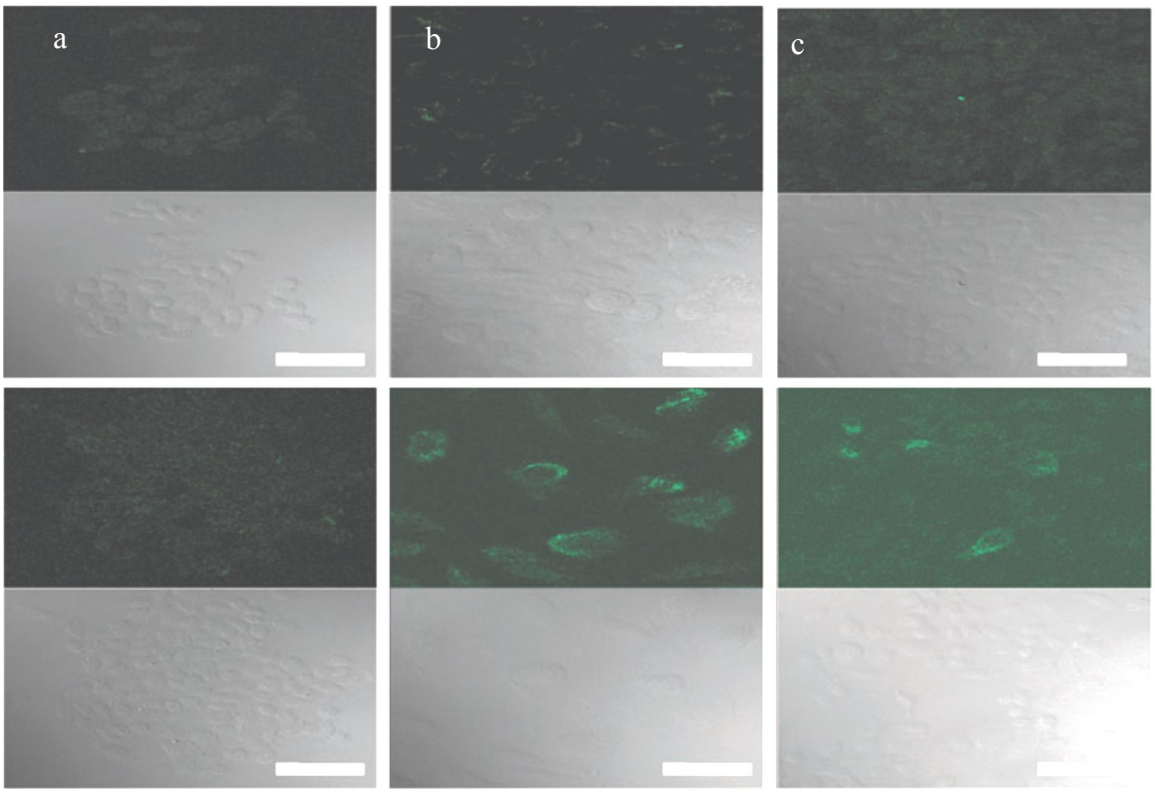

Figure 3: Cell Imaging using Tenascin Targeting Cdots.[41] Confocal microscopy images for CHO (a), HeLa (b), and C6 (c) cells with excitation at 488 nm. The top row of images correspond to cells incubated in thiolated Cdots before aptamer conjugation and the bottom row shows the cells after incubation in the aptamer-Cdots.[41]

In 2012 Barman and Sadhukhan first reported that Cdots could be used to detect Hg^{2+} ions in water.[43] They showed that when Hg^{2+} ions were added to a solution of Cdots the fluorescence was quenched.[43] Several metal cations were also tested and it was shown that the Cdots fluorescence was highly sensitive and selective to Hg^{2+} ions.[43] Although, there was a small amount of quenching observed for Cu^{2+} and Ni^{2+} as well.[43] Zhai et al. also demonstrated this relationship, except the Cdots they produced showed sensitivity to Fe^{3+}, which was not one of the ions tested in the above mentioned study (see Figure 5).[44] Wang et al. used the quenching effect of Cu^{2+} as a probe for glutathione.[45] When glutathione was added to a solution containing Cdots and Cu^{2+}, the quenching effect of the Cu^{2+} was reduced because of the interaction between the glutathione and the Cu^{2+}.[45] This interaction restores the fluorescence of the Cdots allowing one to determine the concentration of the glutathione.[45]

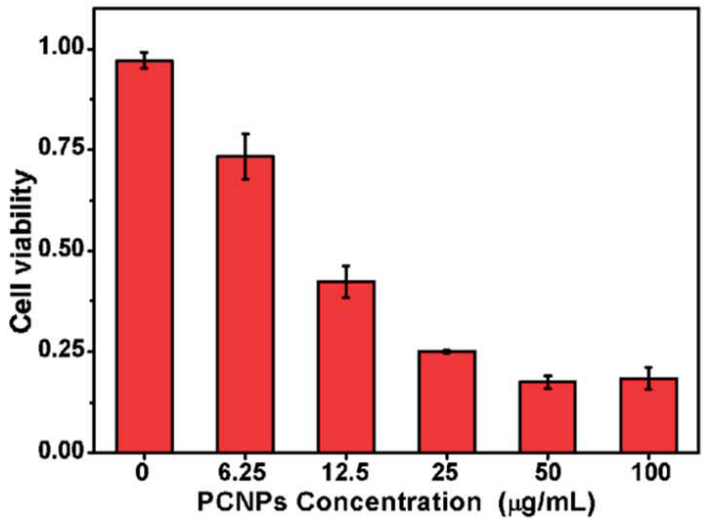

Figure 4: Cell Viability of MCF-7 Cells after Photothermal Therapy using PEGylated CNPs.[10] Cells were incubated with PEGylated CNPs for 24 hours and irradiation with an 808 nm laser for 5 min.[10]

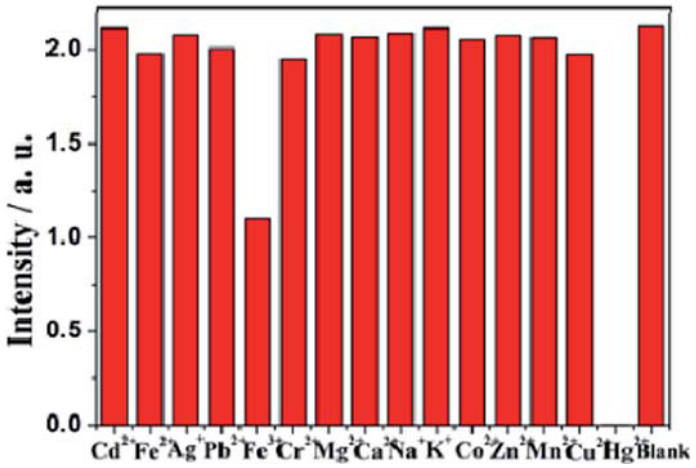

Figure 5: Heavy Metal Detection by Quenching of Cdot Fluorescence.[44]

There are several other interesting applications of Cdots found in the literature. Plants can be grown in a solution of Cdots, allowing the plants to fluoresce. For example, Zhei et al. grew bean sprouts in a Cdot solution giving them a blue glow under ultraviolet light.[44]

Cdots have also found use in electronic devices. Mao et al. used Cdots as the light emitting material in white light emitting diodes.[18] Also, there are many reports of the particles being used in solar cells as the light harvesting medium. [19-20, 22, 24]

Cdots and CNPs have a wide range of uses. Their fluorescence and low cell toxicity allow for them to be used in many biological applications such as imaging and photothermal therapy. The wide bandwidth of fluorescence wavelengths exhibited by Cdots gives them the ability to be used in light emitting diodes and solar cells. The quenching of their fluorescence allows for highly sensitive detection metal cations and molecules that interact with these metal cations. Some of these applications will be explored with the synthesized CNPs in later chapters.

1.3.0 Current Synthesis Methods

There have been many ways to produce Cdots developed over the past few years.[1-35, 46-52] These methods have used a large variety of carbon sources. Cdots were first reported in 2004. Where they were found in the soot of an arc-discharge synthesis method of making single walled carbon nanotubes.[3] They were an unintended byproduct found in the purification step.[3]

Some of the early methods were not cost effective. An example of this is the complex and energy inefficient method requiring laser ablation of a graphite carbon source reported in 2006.[53] The particles produced were carried by a water vapor and argon gas mixture and bubbled through a 900 °C water bath under 75 kPa of pressure.[53] The carbon particles were then refluxed for 12 hours in concentrated nitric acid.[53] They then used various polymers to passivate the surface and the carbon particles became fluorescent.[53] This passivation required heating the particles for another 72 hrs.[53]

A similar method using dibasic ethylenediaminetetraacetic acid (EDTA) has been reported.[39] Small droplets of an EDTA solution were made using a ultrasonic nebulizer and passed through a 550 °C furnace by a carrier gas.[39] The Cdots produced in the furnace were then collected by bubbling the carrier gas through an unspecified liquid, presumably water.[39]

Recently, Hu et al. reported the production of Cdots from coal and coke.[54] The coal was pretreated by heating temperatures ranging from 0 to 1500 °C to produce carbon sources for the Cdot production.[54] The carbon sources were then sonicated in 6 M HNO_3 for 2 hrs and heated for 24 hrs at 140 °C.[54] They also tested the relationship between the size of the particles and the temperature used to pretreat the coal.[54] Their findings

showed that the size of the particles increases slightly with increasing pretreatment temperature.[54] The average size for the Cdots made from coal, with no pretreatment, was 1.96 ± 0.73 nm and the average size from the coal pretreated at 1500 °C was 3.10 ± 0.80 nm.[54] From these numbers, it can also be seen that the size distribution was quite narrow. This method still requires the use of harsh chemicals and high temperatures.

Researchers have also developed a wide array of methods requiring much less energy. To reduce the energy requirements, researchers focused on production and passivation in a single step. Liu et al. used a household microwave to produce Cdots.[36] They dissolved polyethyleneimine (PEI) and glycerol in a buffer solution and heated.[36] This method greatly reduces the amount of energy and time required to produce Cdots. This method was attempted and it was found that upon heating that PEI displays fluorescence properties similar to Cdots. Also, PEI is a very viscous polymer when in solution with water making it very difficult to separate the Cdots from the polymer.

Recently a very low cost and energy efficient method has been reported by Li et al.[55] In this report, it has been shown that by simply mixing two solutions of 0.50 M fructose and 0.50 M NaOH, Cdots can be produced.[55] The reaction was carried out at room temperature, which is a major attribute to keeping costs low. It is unclear at this point to the yield of Cdots produced by this method.

There has also been much research into using "green" carbon sources. These carbon sources are generally plant based.[13] It is believed that since these carbon sources are renewable, these methods are better for the environment.

Wang et al. reported that they were able to make Cdots from eggshells in 2012.[45] They removed the membrane from the eggshells and heated it in a furnace at 400 °C for a

couple of hours.[45] They took the ashes from the furnace and added it to a NaOH solution.[45] This mixture was then heated in a household microwave.[45]

Other "green" precursor include such materials as waste paper, ascorbic acid, many carbohydrates, plant matter, proteins, and meat. [6, 11, 13, 38, 49] It seems that Cdots can be made from nearly any carbon source when heated. All of which require heating the material from 80 to 500 °C, except for the above mentioned room temperature method.

The example synthesis methods listed above show the variety of methods available for making carbon dots. Hydrothermal is the most reoccurring procedure seen in the literature. Many of these procedures use microwaves to heat the precursors. The use of microwaves greatly reduces the time spent heating. Temperature control is difficult when using a household microwave and can be easily controlled with a microwave digester, but these digesters can be quite expensive. Other methods using furnaces often require temperatures higher than 300 °C. Others still, require complicated apparatuses such as laser ablation and aerosol flow systems. The methods proposed in this thesis makes use of a sealed reaction vessel which may not be as readily available as a household microwave, but has better temperature control and requires moderate temperatures. This will be covered in depth in the experimental section of Chapter 2.

1.4.0 Research Objectives

This research was started with the intent to use a previously developed synthesis method to produce Cdots and use them in novel applications. As often happens in research, the goals quickly shifted to developing a novel carbon nanoparticle synthesis

method, purification techniques, and application. To the best of my knowledge, they will be reported for the first time herein.

When this project began in 2013, the number of publications was limited to a few hundred. Now if you search carbon quantum dots or carbon nanoparticles on SciFinder® you will find approximately 2000 papers. Much research has been conducted on these materials in recent years.

The need existed for a method that is able to produce gram-scale quantities of Cdots. The method this research began with, made use of PEI and glycerol, but upon heating the PEI became fluorescent and it was felt that this would interfere with analysis of the Cdots produced. To eliminate this interference, a method was developed to produce Cdots from glycerol alone without the aid of any polymer surface passivation. Ultimately, this method produced CNPs with average size around 80 nm in diameter.

Most methods use dialysis for the purification of the Cdots. This can be quite time consuming and thus, a new method was needed to keep costs, energy requirements, and workup time low. Therefore, a new workup method was devised based on the reduced solubility of the Cdots in acidic solutions. This reduces the workup time by days. More details on the synthesis and workup methods will be covered in Chapter 2.

Detection of heavy metals in aqueous solutions by square wave voltammetry was chosen as the application for the CNPs. Our research group has investigated heavy metal detection by electrochemical techniques in the past.[56] They took multiwall carbon nanotubes (MWNT), carboxylated the surface, and bonded cysteine to the carboxylic acid groups. Then the MWNT-Cysteine was cast onto glassy carbon electrodes. These electrodes were then accumulated in solutions containing either Pb^{2+} or Cu^{2+}. The

cysteine would then bind heavy metal ions through coordination chemistry. Lastly, differential pulse anodic stripping voltammetry would be performed.

Heavy metal detection is very important for safe drinking water. The Environmental Protection Agency regulates the amount of many substances in drinking water. The detection of copper, lead, and mercury was tested with the CNPs and the current Maximum Contaminant Levels on these metals are 1.3 ppm, 15 ppb, and 2 ppb, respectively.[57] The goal was to reliably detect concentrations lower than these limits.

CHAPTER 2: MATERIALS AND METHODS

2.1.0 Chemicals and Instrumentation

Many chemicals and instruments were used in this research. Those used for synthesis, characterization, and application of the CNPs will be listed in this section. More specific details on their use will be discussed in later sections.

The glycerol, iron(III) chloride hexahydrate, and lead(II) nitrate were purchased from Acros Organics. Copper(II) nitrate, acetic acid (CH_3COOH), sodium acetate (CH_3COONa), and 1000 ppm copper(II) nitrate reference standard solution was obtained from Fisher Chemicals. 1000 ppm cadmium(II) nitrate and 1000 ppm lead(II) nitrate reference solutions were purchased from Acros Organics, while 10,000 ppm zinc nitrate, 1000 ppm mercury nitrate and 10,000 ppm manganese nitrate were purchased from Ricca Chemical company. The water used for aqueous solutions was deionized by an in house distillation system and will be referred to as DIW.

Ultraviolet-visible (UV-Vis) spectroscopy was carried out on a Perkin Elmer Lambda 650. A Perkin Elmer LS55 Fluorescence spectrometer was used for fluorescence emission study of the carbon nanoparticles. Fourier-transform infrared (FT-IR) spectroscopy was carried out using a Bruker Vertex 70 Infrared spectrometer or an Alpha Attenuated Total Reflection (ATR) infrared spectrometer. Scanning electron microscopy (SEM) images and energy dispersive X-ray (EDS) spectra were obtained using a FEI Quanta 200 scanning electron microscope with an Oxford Inca II EDS detector. Sizing of particles was carried out using ImageJ software and by a light scattering technique employed by the NanoSight LM10. Electrochemical studies were

performed on a Princeton Applied Research VMP-3 potentiostat with a three electrode cell with 0.5 M KCl as the electrolyte. The working electrode was a glassy carbon electrode, the reference electrode was a Ag/AgCl electrode with 1.0 M KCl filling solution, and the counter electrode was a platinum wire.

2.2.0 Carbon Nanoparticle Synthesis

Three methods were developed to synthesize the carbon nanoparticles from glycerol. These methods will be denoted as 1, 2, and 3 while carbon nanoparticles produced from these methods will be denoted as CNPs-1, CNPs-2, and CNPs-3. At least two runs of each method were carried out.

Method 1 combines glycerol and silica to produce CNPs. CNPs were prepared using a Berghof HighPreactor® with a Berghof BTC-3000 temperature controller (see Figure 6). Silica gel was added to glycerol to make a mixture containing 7.7% wt. silica. Then 100 mL of the mixture was heated to a maximum of 163 °C in the high pressure reactor for 4 hours with the temperature set at 300 °C. The CNPs were then separated by washing the silica gel with 1.0 M sodium hydroxide. The resulting CNPs-1 solution was rotary evaporated to reduce the volume and acetone was added to precipitate any dissolved silica. The silica was removed by filtration through a quantitative cellulose filter several times and then a 0.2 micron filter. The filtered solution was then dialyzed using a Pur-A-Lyzer Mega 3500 Dialysis Kit for 1 week against DIW. The purified CDot solution was then reduced to a few milliliters by rotary evaporation and transferred to vacuum drying station to finish drying.

In method 2 phosphoric acid was added in a 1/20 v/v ratio to the 27% wt. silica gel in glycerol mixture (from above) and was heated in the high pressure reactor with the same parameters as above, however the maximum temperature obtained was 187 °C. The CNPs-2 were separated from the silica gel by washing with 1.0 M sodium hydroxide. Then hydrochloric acid was added to this solution to precipitate any dissolved silica. Then ethyl acetate was added to extract the CNPs-2 (see Figure 7). The ethyl acetate was then removed by rotary evaporation and then vacuum drying.

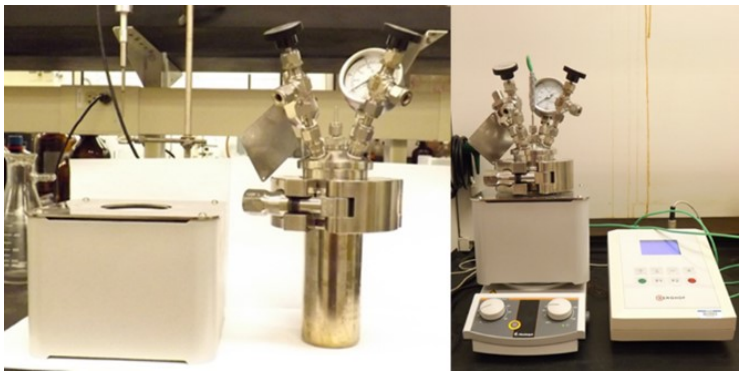

Figure 6: Images of the Berghof High Pressure Reactor. Left image shows the aluminum heating block and the reaction chamber and the right image shows the apparatus assembled with the Berghof BTC-300 temperature controller.

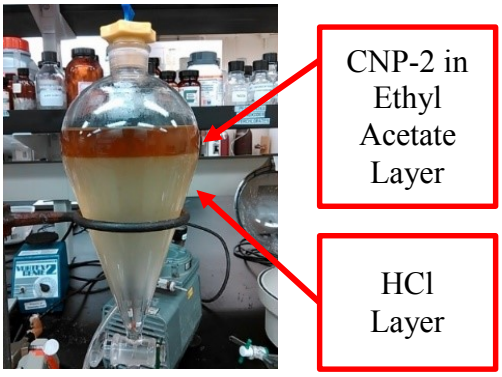

Figure 7: Extraction of CNPs-2 using Ethyl Acetate. The lower layer contains acidified water, in which CNPs have low solubility. An emulsion can be seen in the bottom layer. The top layer contains CNPs suspended in the ethyl acetate.

For method 3, glycerol and phosphoric acid were combined in a 1/20 v/v ration and placed in the Berghof HighPreactor. The temperature was set to 250 °C and the reaction was carried out for 4 hours. The resulting solid product was removed and was then passed through a silica gel column. The first eluent was DIW and the second eluent was methanol. Two distinct bands were collected for both eluents (see Figure 8). The water fractions were set aside and the solvent was removed from the methanol fractions by rotary evaporation and vacuum drying. The dried products were characterized and used for applications.

Figure 8: Fractions Obtained from Column Chromatography of CNPs-3. From the left side of the image, the eluent for the first three flasks was water, the next two was methanol, and the eluent for the last flask was ethyl acetate.

2.3.0 Characterization

The CNPs from each method were characterized by a number of instrumental techniques. The purpose of characterization was to learn their physical and chemical properties. Many of the experiments below were meant to elucidate the chemical structure of the particles. The following sections will outline the procedures used for each instrument.

2.3.1 Fourier-Transform Infrared Spectroscopy. The FT-IR spectra of the CNPs-1 and CNPs-2 were collected on the Bruker Vertex 70 infrared spectrometer. KBr pellets were prepared containing a few milligrams of the sample. The instrument was configured to scan from 400 to 4000 cm^{-1}.

The FT-IR spectrum for the CNPs-3 was collected on a Bruker Alpha ATR infrared spectrometer. The dry powder sample was placed directly onto the crystal and pressure was applied by the built in clamp. The sample was then scanned from 400 to 4000 cm^{-1}.

2.3.2 X-ray Diffraction Spectroscopy. The XRD analysis was performed by Ariful Haque, Md Abdullah-Al Mamun, and their graduate research advisor Dr. Kartik Ghosh. Samples of the CNPs-1, CNPs-2, and CNPs-3 were cast on glass microscope slides. This was accomplished by placing droplets of CNP solutions on the glass slides. All were cast from DIW.

2.3.3 Scanning Electron Microscopy with Energy Dispersive X-ray Spectroscopy. Samples were prepared by casting onto a silicon wafer. CNPs-1 were cast from water, while CNPs-2 and CNPs-3 were cast from methanol or acetone for solubility reasons. Before casting the samples were sonicated for at least 5 min. To help prevent aggregation while castings were drying, the droplets were drawn off of the wafer by lightly touching a lint free towel or paper towel to the edge of the droplet. The wafers were placed in a FEI Quanta 200 Field Emission Gun SEM. The detector used was an Everhart-Thornley detector.

To size the particles using the SEM images, ImageJ was used. ImageJ is a free software provided by the National Institute of Health. This software was obtained from

http://imagj.nih.gom/ij. To measure particle diameters, the scale bar on the SEM images was used to relate its labeled distance to the number of pixels it spans. The software has this feature built into it. Then lines were drawn across the particles along their widest dimension and the software converts the number of pixel this line spans into a distance relative to the scale bar.

To perform EDS on the CNPs-2, they were cast onto a sapphire disk. Then SEM images and an EDS spectrum were acquired. The instrument was calibrated to the silicon peak using a silicon wafer.

2.3.4 Light Scattering Size Determination. A dilute aqueous solution of CNPs-3 was prepared by a number of steps. First a 26 mg/mL CNP-3 aqueous solution was prepared in DIW and sonicated for 15 min. Second, the solution was centrifuged for 15 min at 1000 rpm. Then the solution was filtered with 0.2 μm filter and 0.1 μm filters successively. Finally, the solution was diluted with DIW until the concentration reached the instrument requirement of around 10^8 particles per mL. The dilution was tested by placing the solution, via syringe, into the sample cell of the NanoSight LM10 instrument and performing the analysis. The instrument estimates the concentration which is then displayed. Five runs were performed on the solution and averaged together.

2.3.5 Ultraviolet-Visible Absorbance Spectroscopy. To collect the UV-Vis absorbance spectra of CNPs-1, CNPs-2, and CNPs-3, the samples were suspended in 1.0 M KOH or NaOH. 1.0 M KOH or NaOH was used as a blank for the instrument. Both were placed in a quartz cell and the absorbance was measured from 800 to 250 nm. Spectra were collected on the Perkin Elmer Lambda 650 spectrophotometer.

2.3.6 Fluorescence Spectroscopy. All fluorescence spectra were taken on a Perkin Elmer LS55 Fluorescence spectrometer. Dilute solutions of CNPs-1, CNPs-2, and CNPs-3 were made in 1.0 M NaOH. These solutions were then placed in a quartz cell and the fluorescence spectrum was collected from 380 to 800 nm with the excitation wavelength at 375 nm.

To test how the fluorescence changes with pH, CNPs-2 were suspended in both acidic and basic solutions. The acidic solution was prepared by adding HCl dropwise until the pH of the solution reached 3. The basic solution was prepared in the same manner, with the HCl being replaced with NaOH to obtain a pH of 10. These two solution were then placed in a quartz cell and the fluorescence was measured from 380 to 600 nm with the excitation wavelength set to 375 nm.

The effect of excitation wavelength on the fluorescence spectra was also tested. This was accomplished by making a solution of 0.3 mg/mL of CNPs-1 in DIW. Then fluorescence spectra were collected with the following excitation wavelengths: 300, 350, 400, 450, 500, and 550 nm. Each spectrum was scanned from 20 nm above the excitation wavelength to 800 nm.

To test the effect of concentration on the fluorescence spectrum, several solutions of varying concentration of CNPs-1 in DIW were prepared. These concentrations were: 0.01, 0.05, 0.10, 0.25, 0.50, 1.25, 2.50, and 5.00 mg/mL. The fluorescence spectra of these solutions were obtained by exciting the solutions at 375 nm and recording the spectra from 380 to 700 nm for solutions up to 1.25 mg/mL and from 380 to 800 nm for the solutions of 2.5 and 5.0 mg/mL.

2.4.0 Electrochemical Detection of Heavy Metals

The CNPs were used to detect Cu^{2+}, Hg^{2+}, and Pb^{2+} ions in aqueous solution. The general procedure for square wave voltammetry (SWV) detection of heavy metals will be outlined in this section. The first step is to cast CNPs onto a glassy carbon electrode (GCE) and heat treat this modified GCE. Second, the modified GCE is accumulated in a metal analyte solution. Third, the electrode is placed in the three electrode cell and a constant reduction potential is applied for an amount of time. Finally, SWV is performed. Optimization of these steps will be covered in the following sections.

Several stock solutions were prepared and used for the various tests found in the following sections. Any solution not made from the following stock solutions will be described in the section where they were used. A stock 1000 ppm Cu^{2+} in 1.0 M solution was prepared by dissolving solid CH_3COONa in a 1000 ppm Cu^{2+} in 2% HNO_3 solution. Any solution made from this stock solution will be denoted with "in 1.0 M CH_3COONa."

Another stock solution was prepared containing 10,000 ppm Pb^{2+} in 1.0 M CH_3COONa. This solution was prepared by dissolving solid CH_3COONa and $Pb(NO_3)_2$ in DIW. Any solution made from this stock solution will be denoted with "in 1.0 M CH_3COONa."

A second 1000 ppm Pb^{2+} stock solution was prepared by dissolving solid $Pb(NO_3)_2$ in DIW. Solution prepared from this stock solution will be denoted simply by their Pb^{2+} concentrations in ppm.

2.4.1 Potentiostat Apparatus. The SWV was carried out using a Princeton Applied Research VMP3 Potentiostat. All runs were carried out in a three electrode cell. The three electrodes were the GCE modified with CNPs as the working electrode, the

Ag/AgCl reference electrode with 1 M KCl filling solution, and the Pt wire counter electrode (see Figure 9). The electrolyte solution was either 0.5 M KCl or 1.0 M CH_3COONa, which was both deoxygenated and stored with Ar before runs. The GCEs were cleaned before each run by washing with acetone and then polishing with 1.0 and 0.05 micron alumina for 20 seconds each. Then the alumina was washed away in an ultrasonic bath.

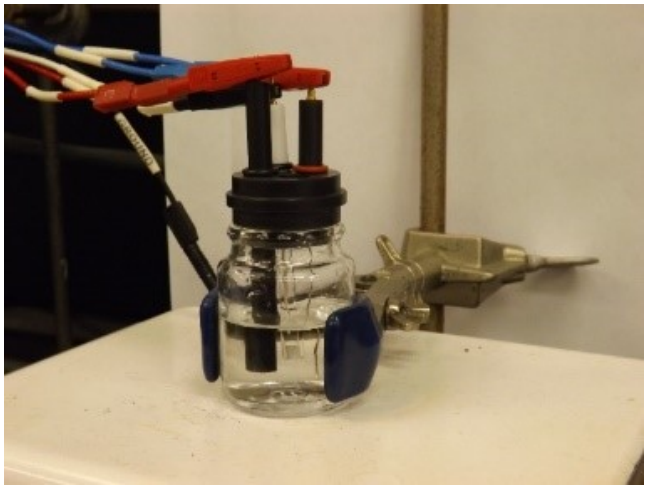

Figure 9: Image of the Three Electrode Cell used for SWV Analysis. The electrodes from left to right were: CNP modified GCE working electrode, Ag/AgCl reference electrode with 1 M KCl filling solution, and Pt wire counter electrode.

2.4.2 Accumulation Optimization. Accumulation is the process of depositing the metals onto the CNP modified GCEs. This was accomplished by suspending the electrodes in solutions containing metal ions (see Figure 10). The amount of time the electrode spends in the solution is important for maximum peak current.

To optimize the accumulation time 10 μL of a 95 mg/mL aqueous suspension of CNPs-2 was drop-cast onto the electrode and allowed to dry at atmospheric conditions.

Then the electrodes were dipped in a 100 ppm Pb^{2+} solution, made by diluting a 1000 ppm $Pb(NO_3)_2$ in 2% HNO_3 solution with 0.10 M CH_3COONa, for times ranging from 5 to 35 min in 5 min increments. Three runs were performed for each accumulation time. Then cyclic voltammetry was performed by scanning the potential from -1.6 V to 1.0 V and back to -1.6 V at a rate of 50 mV/s in the three electrode cell. All accumulations were performed while stirring at 100 rpm, here and throughout the rest of this thesis. Also, after accumulation the electrodes were washed by dipping in DIW and drawing the water off using a lint free towel.

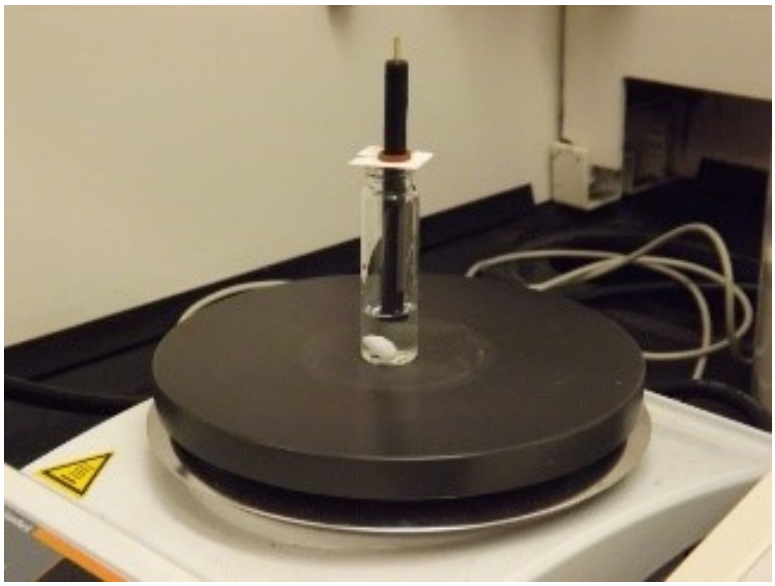

Figure 10: Image of Accumulation Setup. The electrode was suspended in the metal analyte solution and stirred at 100 rpm for 20 min.

2.4.3 Optimization of Electrode Preparation. Electrodes were prepared for heavy metal detection by taking pre-cleaned and polished GCE electrodes and modifying them with CNPs by drop casting a solution containing CNPs. This was a very long

process and many variations were attempted, but here I will report on the procedures for preparing the modified GCE electrodes used for actual metal detection studies.

To stabilize the CNP castings, the modified electrodes were heat treated in a 190 °C oven. The time spent in the oven was optimized by casting 0.52 mg of CNPs-3 onto the GCE by drop casting a 26 mg/mL CNP-3 suspension in 10 μL increments. Several of these electrodes were prepared and placed in the oven for 0.5, 1.0, 1.5, 2.0, and 3.0 min. Next, they were accumulated in a 100 ppm Cu^{2+} in 1.0 M CH_3COONa solution for 20 min. Then SWV was performed with the following parameters: reduction potential = -1.0 V, reduction time = 5 min, pulse height = 200 mV, pulse width = 2.0 ms, and step height = 0.5 mV.

Electrode preparation for the detection of copper was optimized by drop casting a 26 mg/mL aqueous suspension of CNPs-3 onto GCE in 10 μL increments to give the following CNP masses: 0.26, 0.52, 0.78, 1.0, and 1.3 mg. Then these electrodes were placed in a 190 °C oven for 1 min. Next, the electrodes were accumulated in a 100 ppm Cu^{2+} in 1.0 M CH_3COONa at pH 5.98 for 20 min. Then SWV was performed with the following parameters: reduction potential = -1.0 V, reduction time = 5 min, pulse height = 200 mV, pulse width = 2.0 ms, and step height = 0.5 mV.

The optimization of electrode preparation for the detection of lead was performed following the same procedure found above for copper with some differences. The masses tested were: 0.52, 1.4, 1.6, 2.1, and 2.6 mg. Also, the electrodes were accumulated in 100 ppm Pb^{2+}.

2.4.4 Optimization of SWV Parameters. The reduction time was optimized by suspending a CNP-3 modified GCE in a 100 ppm Cu^{2+} in 0.10 M CH_3COONa solution at

pH 5.98 (made by diluting a 1000 ppm Cu^{2+} in 2% HNO_3 solution with a 0.10 M CH_3COONa solution) for 20 min and then applying a reduction potential of -1.0 V for various amounts of time. These times spanned from 1-5 min in 1 min increments. Then SWV was performed with the following parameters: pulse height = 100 mV, pulse width = 2.0 ms, and step height = 0.5 mV. The step potential was scanned from -1.0 to 1.0 V at 125 mV/s.

The optimization of the SWV pulse height was carried out using a 100 ppm Pb^{2+} in 1.0 M CH_3COONa solution. CNP-3 modified GCEs were heat treated for 1 min and accumulated in this solution for 20 min. Then SWV was performed with pulse heights of 100, 200, 250, 300, and 500 mA. The SWV parameters were: pulse width = 2.4 ms, step height = 0.5 mV, reduction time = 5 min, and reduction potential = -1.0 V. The step potential was scanned from -1.0 to 1.0 V at 104 mV/s.

The pulse width was optimized by suspending a GCE, modified with CNPs-3 and heat treated for 1 min, in a 10 ppm Pb^{2+} in 1.0 M CH_3COONa at pH 5.98 solution and performing SWV with pulse widths of 0.4, 1.0, 1.4, 2.0, 2.4, 3.0, 3.4, 4.0, and 5.0 ms. The other SWV parameters were: pulse height = 200 mV, step height = 0.5 ms, reduction potential -1.0 V, and reduction time = 5 min. The step potential was scanned from -1.0 to 1.0 V at 104 mV/s.

2.4.5 Optimization of Accumulation pH. Solutions containing 100 ppm Cu^{2+} with two concentrations of CH_3COOH/CH_3COONa buffer. 100 ppm Cu^{2+} solutions were made by diluting a 1000 ppm Cu^{2+} in 2% HNO_3 with 0.10 M CH_3COOH/CH_3COONa buffer. Several ratios of CH_3COOH to CH_3COONa solutions were prepared and they were: 100/0, 80/20, 50/50, 20/80, and 0/100. The pH of each of these solutions was

recorded. A second set of 100 ppm Cu^{2+} solutions were prepared by dissolving solid $Cu(NO_3)_2 \times 2.5\ H_2O$ in 1.0 M CH_3COOH/CH_3COONa buffer solutions with pH values of 5.5, 5.98, and 7.65. Then CNP-3 modified GCEs were accumulated in each solution for 20 min and cyclic voltammetry was performed. The voltammogram was collect by scanning the potential from -1.5 to 1.0 and back to -1.0 V.

Analysis of this data was carried out using the Henderson-Hasselbalch equation. This was used to calculate the equilibrium concentrations of CH_3COOH and CH_3COO^- in the buffer solutions based on their pH and starting molarity. That is:

$$pH = pK_a + \log([CH_3COO^-]/[CH_3COOH])$$

and the *pH* was determined experimentally, the pK_a of CH_3COOH is 4.76, and $\log([CH_3COO^-]/[\ CH_3COOH])$ is the $\log[(1.0\ M - x)/x]$ for the 1.0 M solutions and the $\log[(0.10\ M - x)/x]$ for the 0.1 M solutions. Then by solving for *x*, the concentration of CH_3COOH can be found and then the concentration of $CH_3COO^- = 1.0 - x$ or $0.1 - x$ depending on the solution.

2.4.6 Calibration Curves. Several attempts at calibration curves were attempted for the detection of copper, mercury, and lead using SWV. In this section the parameters used to obtain these calibration curves will be discussed. Some parameters will be consistent between all curves while some will be changed. The changes made will be in an attempt to increase the sensitivity of the calibration curves and therefore the detection limits.

The SWV parameters were set to: pulse height = 200 mV, step height = 0.5 mV, pulse width = 2.4 ms, reduction time = 5 min, and reduction potential = -1.0 V for all calibration curves, except for the first copper and mercury calibration curves where the

pulse width was 2.0 ms. The 2.0 ms pulse width was based on preliminary data that was superseded by repeat experiments. The CNP-3 modified GCES underwent 1.0 min of heat treatment at 190 °C throughout the experiments. Also, the electrolyte solution in the three electrode cell was 0.5 M KCl for all SWV runs except for the second and third lead calibration curve.

The calibration curves for copper were performed with different amounts of CNPs-3 cast onto the GCE. For the first calibration curve the amount cast was 0.5 mg and for the second calibration curve 1.0 mg. For both calibration curves the accumulation solutions were made using the 1000 ppm Cu^{2+} in 1.0 M CH_3COONa solution from above. The pH of these solutions was adjusted to 5.98 using 1.0 M CH_3COOH. This was accomplished by preparing a 1.0 M CH_3COOH/CH_3COONa buffer solution of the desired pH and using it to dilute the Cu^{2+} solution.

The mercury calibration curve used the same parameters as the second copper calibration curve. The only difference was the accumulation solutions. These solutions were prepared using a stock solution made with a 1000 ppm Hg^{2+} in 3% HNO_3 solution and dissolving solid CH_3COONa into this solution to make a 1000 ppm Hg^{2+} in 2.0 M CH_3COONa. This stock solution was diluted using a 2.0 M CH_3COOH/CH_3COONa buffer at pH 5.98.

Three lead calibration curves were collected and each had significant differences between them. The differences were the amount of CNPs-3 cast, accumulation solutions, electrolyte solution, and the pulse widths of the SWV. The amount of CNPs-3 cast for the first and second calibration curve was 0.5 mg and for the third calibration curve was 2.1 mg. The accumulation solutions for the first and second calibration curves were

made using the Pb^{2+} "in CH_3COONa" stock solution from Section 2.4.5. This solution was diluted with a 1.0 M CH_3COOH/CH_3COONa buffer at pH 5.98 to make the accumulation solution for these two calibration curves. The stock Pb^{2+} solution "in DIW" from Section 2.4.5 was used to make the accumulation solutions for the third lead calibration curve (a test of the Pb^{2+} solution was performed by making a 10 ppm Pb^{2+} solution and performing SWV in the same manner as the second lead calibration curve and comparing it to one of the 10 ppm Pb^{2+} in CH_3COONa solution SWV runs from the second lead calibration curve). The electrolyte solution for the first calibration curve was 0.5 M KCl, while the electrolyte solution for the second and third calibration curve was 1.0 M CH_3COONa with pH 4.5. The pH of the 1.0 M CH_3COONa electrolyte solution was optimized by running SWV on CNP-3 modified electrodes that had been heat treated for 1 min and accumulated in 50 ppm Pb^{2+} in CH_3COONa at pH 5.98.

2.5.0 Copper Detection with Changing Temperature

To determine how changes in temperature affect the copper peak current, SWV was performed on CNP-3 modified GCE electrodes that were heat treated for 1 min. They were accumulated in a 100 ppm Cu^{2+} in 1.0 M CH_3COONa solution at pH 5.98. The SWV parameters were the same as for the second copper calibration curve. The exception was that the temperature of the accumulation solutions was changed. This was accomplished by accumulating electrodes in analyte solutions at three temperatures: 8 °C, 18 °C, and 30 °C. To change the temperatures of the accumulation solutions they were placed in either an ice water bath or a warm water bath before and during accumulation. The 18 °C temperature was the air temperature of the laboratory on that day.

2.6.0 Fluorescence Detection of Metals with CNPs

To test if the CNPs could be used to detect heavy metals by quenching of the CNP's fluorescence, 0.30 mg/mL CNP-1 solutions were prepared containing 1.4 mM $LiClO_4$, 1.0 mM $CoCl_2$, 2.5 mM $ZnCl_2$, 1.3 mM $Pb(NO_3)_2$, 1.7 mM $MnCl_2$, and 1.0 mM $FeCl_3$. Then fluorescence spectra were obtained for these solutions and compared to a 0.30 mg/mL CNP-1 solution.

CHAPTER 3: CARBON NANOPARTICLE CHARACTERIZATION

3.1.0 Chemical Analysis of the CNPs

The structure of the CNPs can be determined by several analytical techniques. These include Fourier-Transform infrared spectroscopy (FTIR), X-ray diffraction (XRD), and energy dispersive X-ray spectroscopy (EDS). In this section the results obtained for the CNPs from these methods will be discussed.

3.1.1 Infrared Spectroscopy. FTIR spectroscopy shows the functional groups that can be found in the CNPs. Molecules absorb infrared light and convert that energy to vibrational and rotational energy. Since the strength of the bond is directly proportional to the wavelength of infrared light absorbed, the type of atoms and bonds present can be determined to some degree. Only some vibrational modes are infrared active. These are modes where the dipole moment of the bond or molecule changes.[58] The bond strength combined with only specific vibrational modes being active gives very specific regions where types of bonds lie. For example: an O-H bond of an alcohol or water absorbs infrared frequencies between 3400-3650 cm^{-1}.

The FTIR spectrum of the CNPs-1 showed several functional groups (See Figure 11). One of the strongest peaks is located at 1049 cm^{-1} which was due to the C-O bond of an alcohol. At 1559 cm^{-1} there was a C=C peak. C-H peaks were also present at 1403, 1456, and 2927 cm^{-1}. The C=C peak had a shoulder with many small peaks. These small peaks could be due to either small amounts of various carbonyl groups or aromatic C-H groups. There are also shoulder peaks on both the C-O peak and the O-H peak. This suggests that a small amount of carboxylic acid groups exist in the CNPs-1.

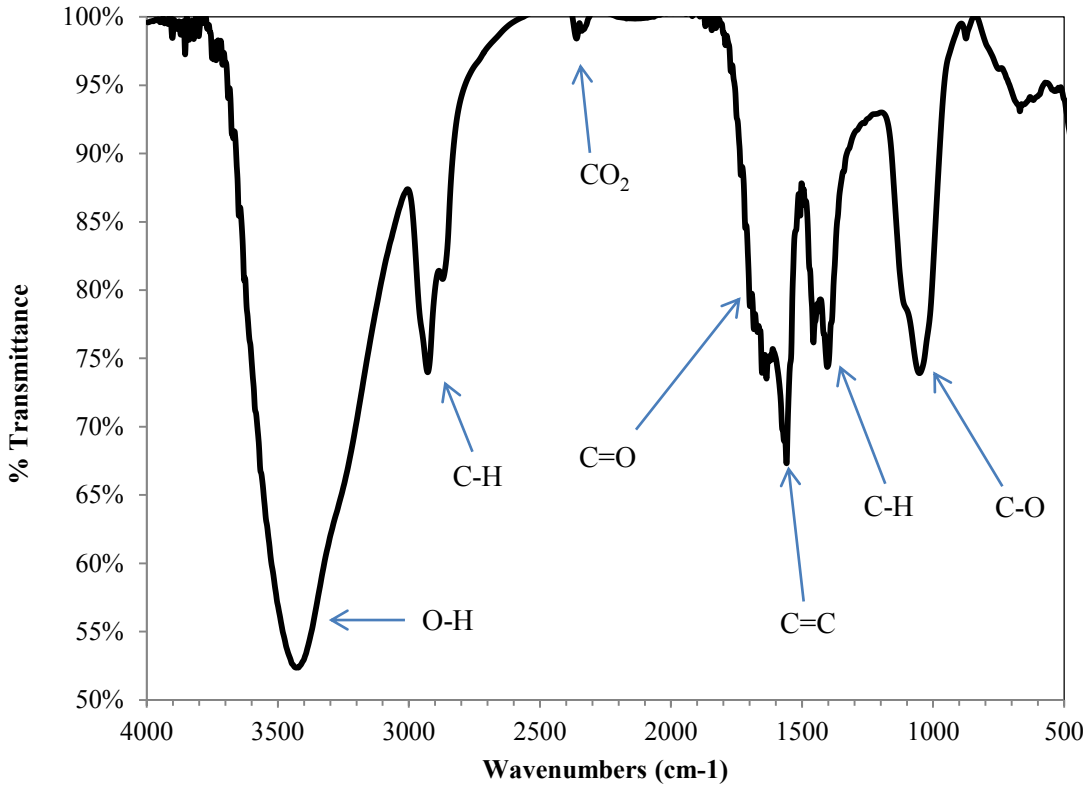

Figure 11: The FT-IR Spectrum of CNPs-1.

The addition of phosphoric acid during the CNP-2 reaction produced CNPs with an interesting FTIR spectrum. Figure 12 shows that there was a large increase in the carbonyl peak, 1708 cm^{-1}, which suggests that the acidic conditions increased the amount of carboxylic acid groups. Also, the presence of a C-O peak at 1206 cm^{-1}, not present in the CNP-1 spectrum, and the broadening of the O-H peak (3200-3600 cm^{-1}) was a clear indication of this increase. The shape of this O-H peak suggests that there were two types of functional groups containing O-H bonds. Other peaks include: a C-O (alcohol) peak at 1108 cm^{-1}, C-H peaks at 1384, 1409, 1454, and 2921 cm^{-1}, and a shoulder on the C=O peak that is probably due to C=C groups.

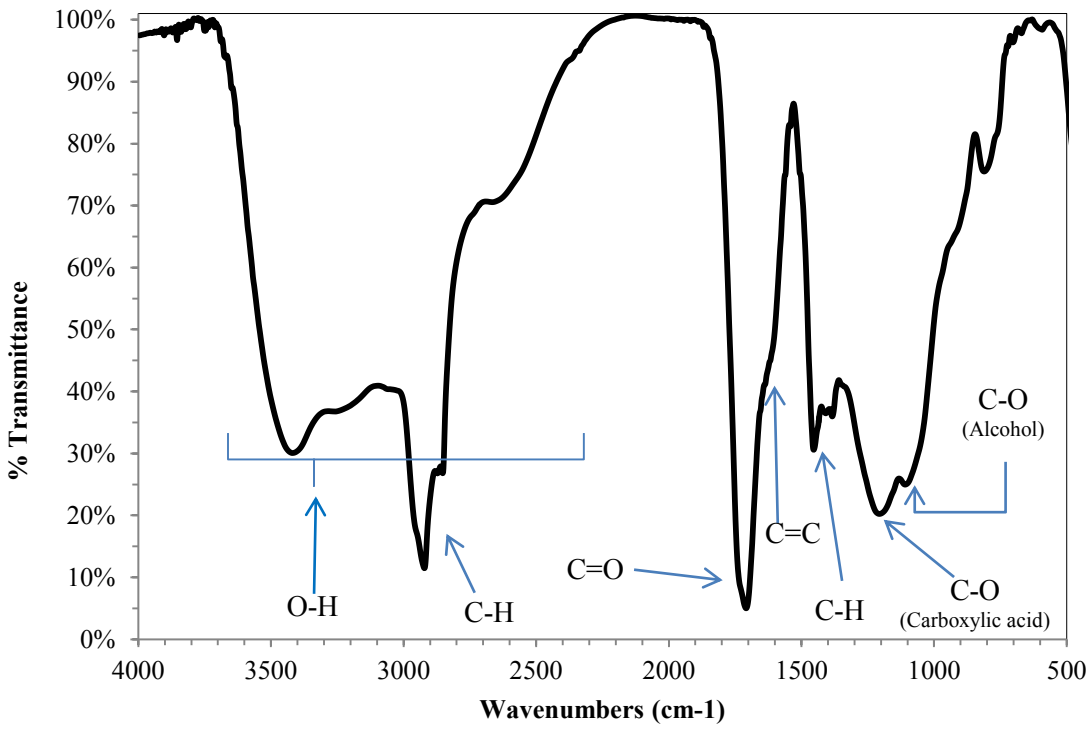

Figure 12: The FT-IR Spectrum of CNPs-2.

The FT-IR data showed that the CNPs have several functional groups present. Both spectra had evidence for the presence of alcohols, alkyl, and unsaturated carbons. It seems that the different reaction conditions produced a larger amount of carboxylic acid groups in the CNPs-2 than in the CNPs-1.

The CNPs-3 FT-IR spectrum after filtration and before vacuum drying was similar to that of the spectrum for the CNPs-2 (see Figure 13). There was the expected C=O peak at 1702 cm^{-1} and C-O peaks ranging from 1047 to 1196 cm^{-1}. The multiple C-O peaks are often present in the spectra of carboxylic acid containing compounds. The large O-H peak at 3372 cm^{-1} seems to be a combination of alcohol and carboxylic acid peaks, since it has a narrow peak around 3400 cm^{-1} and a broad shoulder spanning from around 3300 to 2200 cm^{-1}. This suggests that the C-O bonds of alcohols would contribute

to the C-O peaks as well. It would be expected that the C-O peaks at higher wavenumbers would be due to the carboxylic acids because of partial double bond character from resonance and induction from the C=O bond. Also, there was a shoulder on the C=O peak which may be due to a combination of C=O bonds, from other carbonyl species, and C=C bonds. Finally, aliphatic carbons were present in the material as well and this was shown by the presence of C-H peaks at 1377, 1448, and 2926 cm^{-1}.

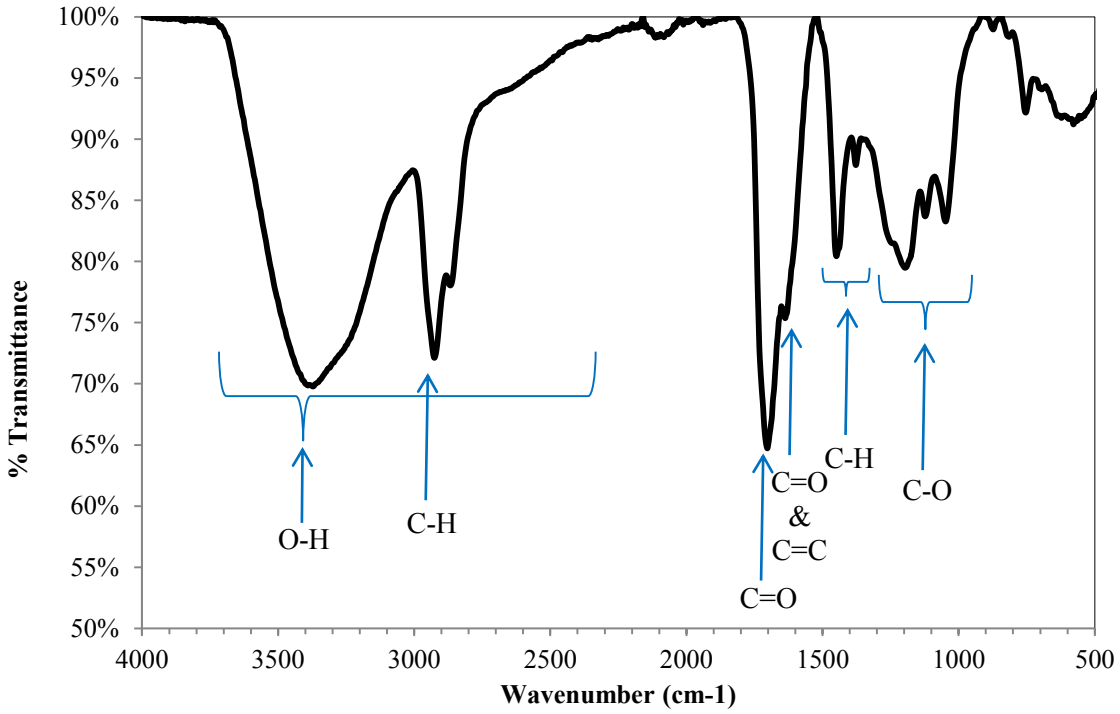

Figure 13: The FT-IR Spectrum of CNPs-3 after Washing with Water and before Vacuum Drying.

After vacuum drying the CNPs-3, the FTIR spectrum showed a reduced O-H peak at 3390 cm^{-1} (see Figure 14). The resulting O-H peak was very broad which tells us that the primary O-H species were carboxylic acids. It also showed that water washing alone was not enough to remove the methanol used in processing. The CNPs retain good

solvents, or solvents that disperse the CNPs well, which may be useful in future applications.

This solvent retention influences the solubility of the CNPs in water. In the protonated form water solubility is reduced already, and with the addition of less polar solvents such as methanol, acetone, and ethyl acetate, they become increasingly hydrophobic, respectively. This limits their ability to be suspend in water to the point where the particles are not wettable for the case where ethyl acetate was retained.

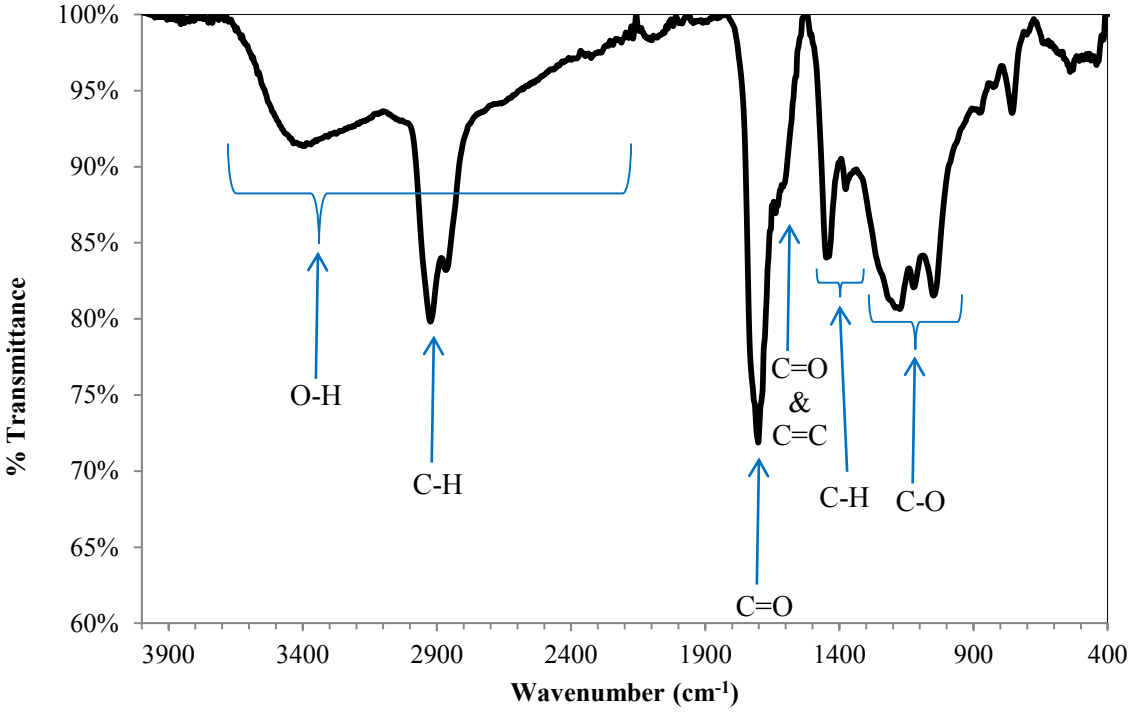

Figure 14: The FT-IR Spectrum of CNPs-3 after Vacuum Drying.

3.1.2 X-ray Diffraction Spectroscopy. X-ray diffraction is a good tool for studying the structure of materials on an atomic level. When X-rays enter a material some are scattered in a specific pattern and when this pattern is analyzed, atom

arrangement can be determined. When the material has a crystalline structure and atoms are arranged in a uniform pattern of parallel layers, the X-rays are scattered at the same angle as long as the distance between the layers is uniform. These rays exiting the material will interact through destructive and constructive interference creating a diffraction pattern. In amorphous materials, the atoms are arranged in a less ordered pattern and, therefore, the distances between atoms is not uniform. This translates into a diffraction pattern that is based on the frequency of interatomic distances, so the peak seen in the pattern is a distribution of the interatomic distances. In crystalline materials the lattice structure can be obtained and in amorphous materials an interatomic distance histogram is obtained.[59]

The relationship between the pattern obtained and the interatomic or interlayer distance is governed by Bragg's law. Bragg's law is a relationship between the interatomic distance, wavelength of incident light, and the angle of incidence such that:

$$n\lambda = 2d \sin\theta$$

where n is an integer, λ is the wavelength of the incident radiation (0.15405 nm in this case), d is the interatomic/interlayer distance, and θ is the angle of incident X-ray relative to the planes of the atomic layers.

The XRD pattern for CNPs-1 is shown in Figure 15. A broad peak at 22.6 2θ degrees is the normal amorphous carbon peak found in carbon nanoparticles. At this angle, the corresponding distance between the atoms would be 0.393 nm. There was also a sharp peak at 32.04 2θ degrees, which suggests that there was a crystalline component to the material with an interlayer distance of 0.279 nm. This suggests that CNPs-1 consisted of both crystalline and amorphous regions.

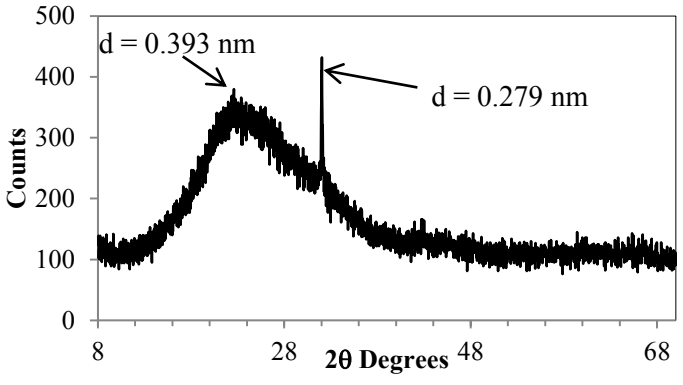

Figure 15: The XRD Pattern of CNPs-1.

The XRD pattern for CNPs-2 in Figure 16 was very similar to that of CNPs-1. Both the amorphous and crystalline peak were shifted slightly toward larger interatomic/interlayer distances. The crystalline peak was at 31.84 2θ degrees, which corresponds to an interlayer distance of 0.281 nm. The amorphous peak was around 21.36 2θ degrees and an interatomic distance of 0.416 nm.

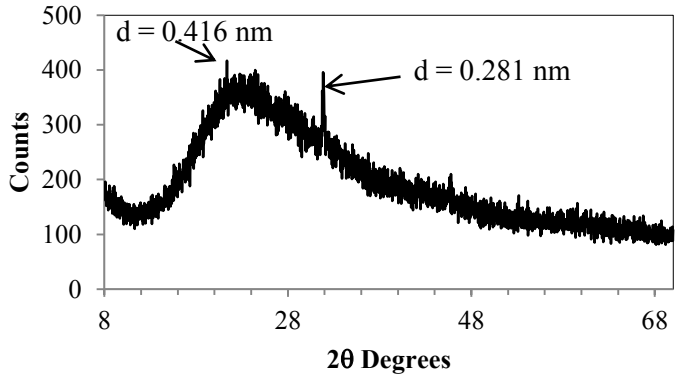

Figure 16: The XRD Pattern of CNPs-2.

Figure 17 shows the XRD pattern for CNPs-3. The crystalline peak was not seen this sample. This may have been due to sample preparation. It was discuss previously,

how the CNP-3 sample was further dried under vacuum, which seems to have eliminated most of the retained solvent. The solvent may form a crystalline region on the surface of the particles by interaction with the functional groups resulting in the sharp peak seen in Figures 15 and 16. Also, the amorphous peak centered around 19 2θ degrees was shifted by about 4 degrees lower than that of CNPs-1 and CNPs-2.

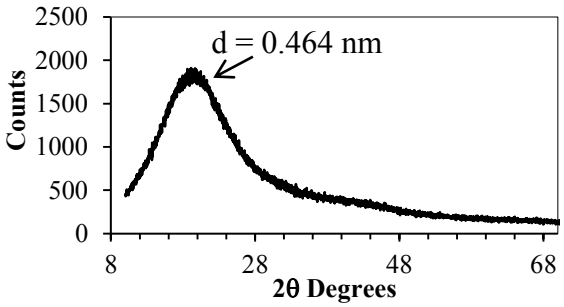

Figure 17: XRD Pattern of CNPs-3.

The XRD patterns for carbon nanoparticles found in the literature show only the amorphous peak. The amorphous peak in the patterns for the CNPs-1 and CNPs-2 is very similar to the patterns found in the literature (see Figure 18). The crystalline peak in the CNPs is very uncommon in carbon nanoparticles from literature.

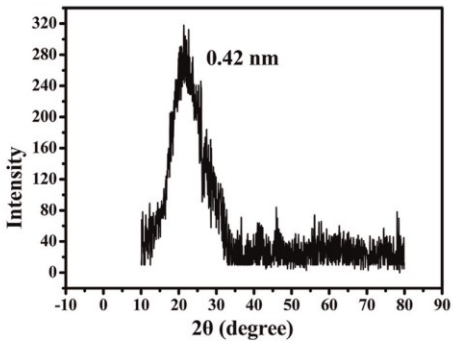

Figure 18: Representative Cdot XRD Pattern from Literature.[60]

3.1.3 Energy Dispersive X-ray Spectroscopy. To determine whether there was any presence of the silica in particles from synthesis or workup, EDS was performed. When electrons bombard a substance, inner shell electrons are ejected. Then upper shell electrons fill the gap left by the removal of the inner electrons.[59] Since the upper shell electron has more energy than the lower shell, the excess energy is given off as an X-ray photon.[59] Elements can be differentiated by their characteristic X-ray emissions.[59]

Normally images of CNPs are taken on a silica wafer, but this would interfere with the experiment, so CNPs-2 were cast from a dilute NaOH solution onto a sapphire disk. The conductivity of the sapphire disk is lower than that of the silica wafer and limits the quality of the images obtained due to charge buildup in the particles. The aluminum peak in the EDS was from the sapphire disk (see Figure 19). This Figure also shows that silica was not present in any measurable amount. Carbon and oxygen are most likely from CNPs-2, while the sodium peak was most likely from the casting solution, but could also be from the workup. Oxygen is also present in the sapphire disk and would add to the oxygen peak as well.

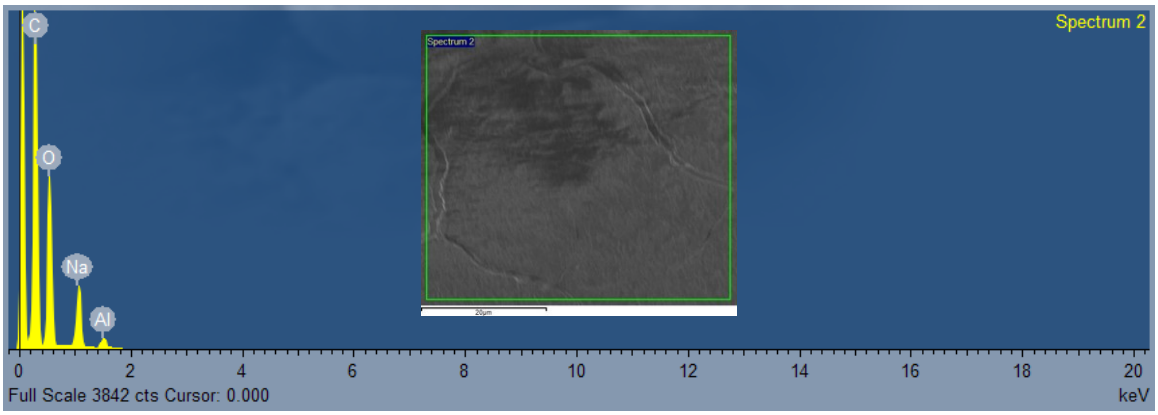

Figure 19: EDS Spectrum of CNPs-2. The EDS spectrum of CNPs-1 and SEM image showing the area scanned to obtain the EDS spectrum (inset).

3.2.0 Particle Size Determination

Scanning electron microscopy (SEM) is a very nice tool to provide evidence of nano-scale dimensions. This instrument consists of an electron source, lens, sample holder, and detector. An electron beam is fired at the sample and focused by the electric field of the lens.[59] The beam is then scanned across the surface of the sample.[59] The incident electrons collide with electrons in the sample in both elastic and non-elastic collisions.[59] Some of these electrons are scattered away from the sample surface and are collected by a detector. The image is collected by counting the number of ejected electrons that hit the detector.[59] The detector used counted the number of secondary electrons (those liberated from the material by non-elastic collisions). This produces a grayscale image with shading being determined by the number of detected electrons.

3.2.1 Scanning Electron Microscopy. Many images of CNPs-1 were obtained for sizing the particles and Figure 20 is a good representative of those images. A large number of particles of various sizes could be seen in this image. The CNPs-1 were spherical particles with an average diameter of 66.4 nm, but they had a large size distribution, spanning from around 30.1 to 260.8 nm (see Table 1). Even with the large size distribution, 95% of the particles were below 100 nm and 44.7% of the particles fell between 56 and 70 nm (see Figure 20).

The CNPs-2 were also spherical particles with the majority having diameters less than 100 nm. The average size of the particles was smaller than the CNPs-1 at 57.7 nm (see Table 1). The shape of the distribution curve was also wider for the CNPs-2 than for the CNPs-1 (see Figure 20). The peak width at half maximum spanned from 28 to 84 nm for the CNPs-2, while it spanned from 50 to 80 nm for the CNPs-1 (see Figure 20).

This was also demonstrated by the standard deviation for the two size distributions, which was 19.4 nm and 24.3 nm for the CNPs-1 and CNPs-2, respectively (see Table 1). It can also be seen in Table 1 that the smallest particles were at 13.4 nm and the largest particles had diameters of 154.9 nm. The CNPs-2 also had a larger amount of particles less than 40 nm. This could be easily seen in the SEM images (see Figure 20).

Table 1: ImageJ Sizing Results for CNPs-1, CNPs-2, and CNPs-3. Data include the sample size, maximum diameter, minimum diameter, average diameter, and the standard deviation of the particle diameter.

ImageJ Particle Sizing Results			
	CNPs-1	CNPs-2	CNPs-3
Sample Size	591	705	782
Maximum Diameter (nm)	260.8	154.9	1669.8
Minimum Diameter (nm)	30.1	13.4	11.5
Average Diameter (nm)	66.4	57.7	80.39
Standard Deviation (nm)	19.4	24.3	117.6

The sizing results for the CNPs-3 were quite different from the other two methods previously discussed above. The average diameter was 80.4 nm (see Table 1), which was close to the other two methods, however this average was skewed more significantly than the other two, by the wide size distribution. With 68 % of the particles at or below 81 nm the majority of the particles were smaller than the average (see Figure 22). The effect of the large size distribution was reflected in the 117.6 nm standard deviation (see Table 1).

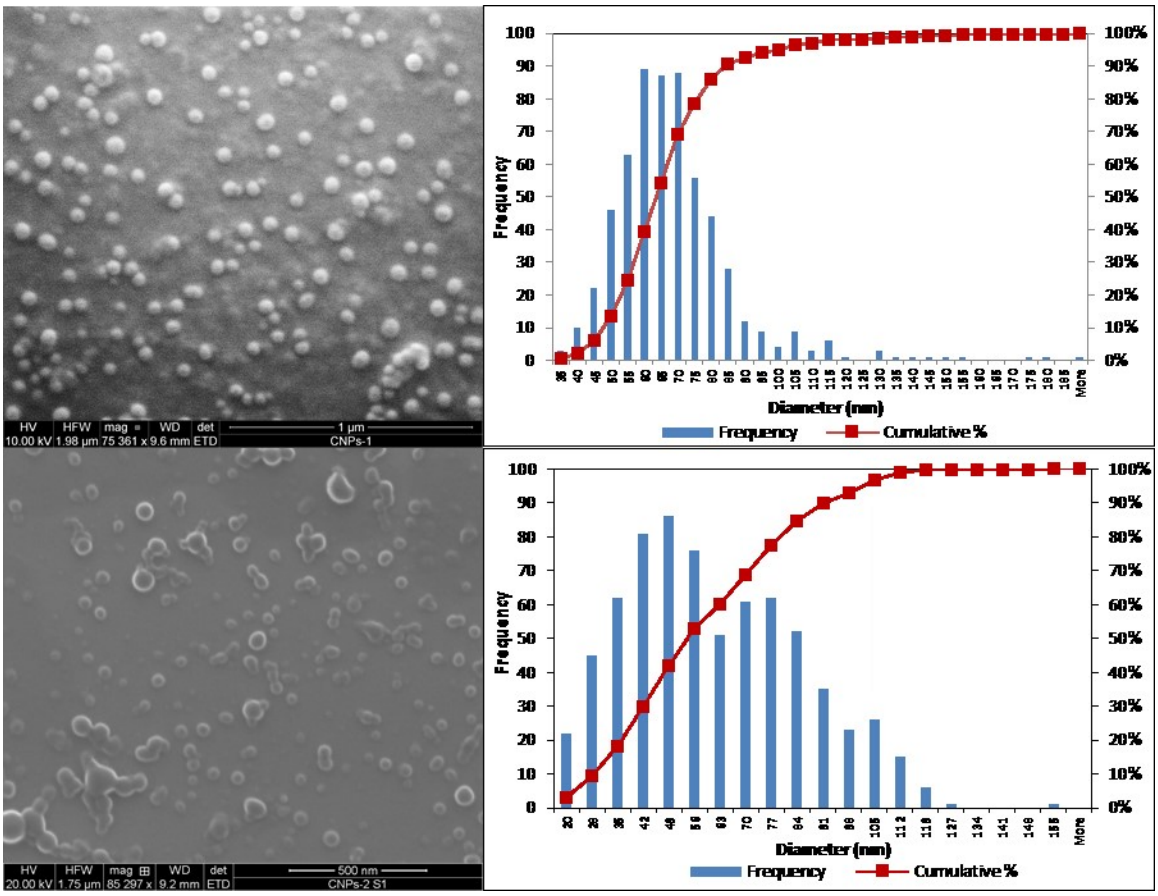

Figure 20: Size Analysis of CNPs-1 and CNPs-2. SEM images in combination with ImageJ were used to size the particles. Representative images can be found here for the CNPs-1 (top left) and the CNPs-2 (bottom left) along with the size distributions for the CNPs -1 (top right) and CNPs-2 (bottom right) are shown here with inset tables showing the sample size, maximum diameter, minimum diameter, average diameter, and the standard deviation of the particle diameters.

The particles found in the SEM images ranged from 11.5 to 1670 nm (see Table 1). The diameter range with the highest frequency was between 21-31 nm (see Figure 21). This diameter was about half of the highest frequency diameter of the CNPs-1 (see Figure 20). The SEM image in Figure 21 showed how significant the amount of these small particles was, while Figure 23 shows a variety of the larger particles.

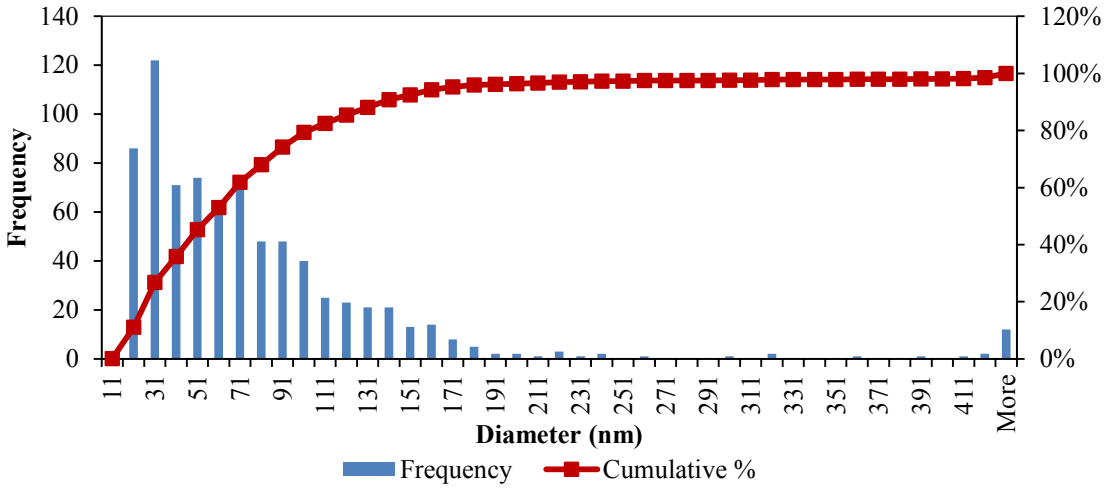

Figure 21: CNP-3 ImageJ Size Distribution. Data obtained from SEM image analysis using ImageJ software.

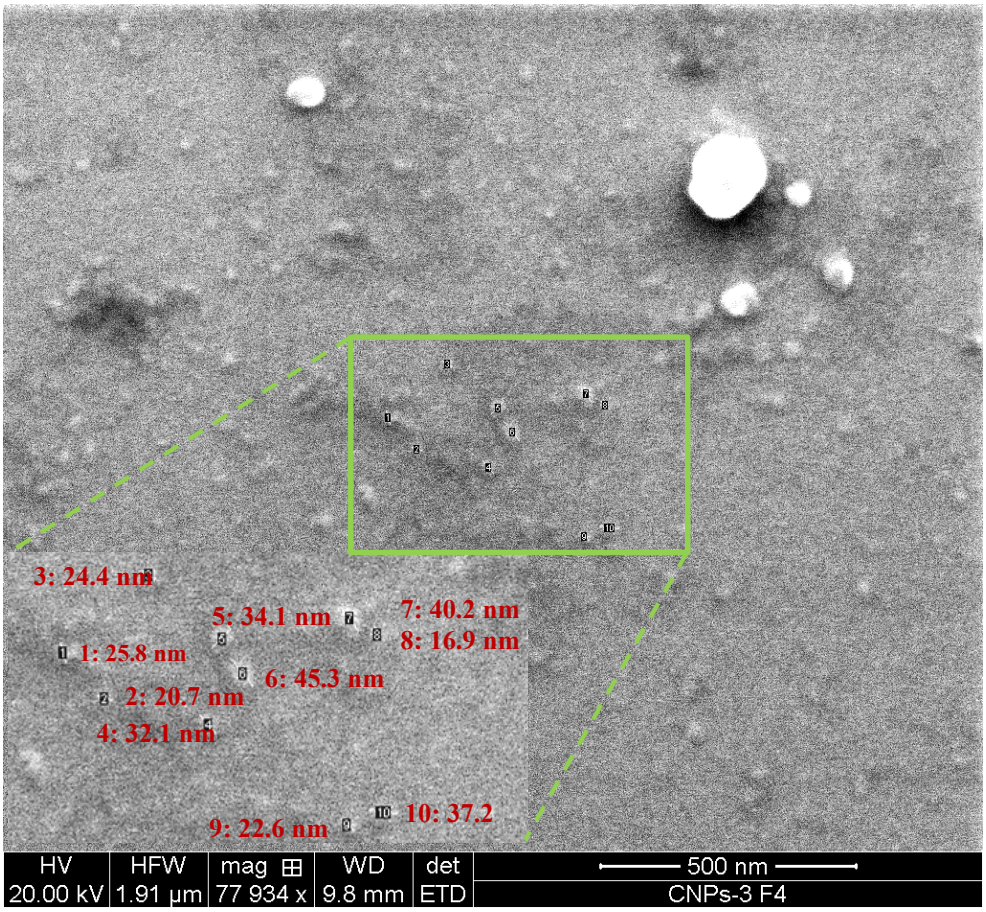

Figure 22: SEM Image of CNPs-3. The labeled particles were sized using ImageJ.

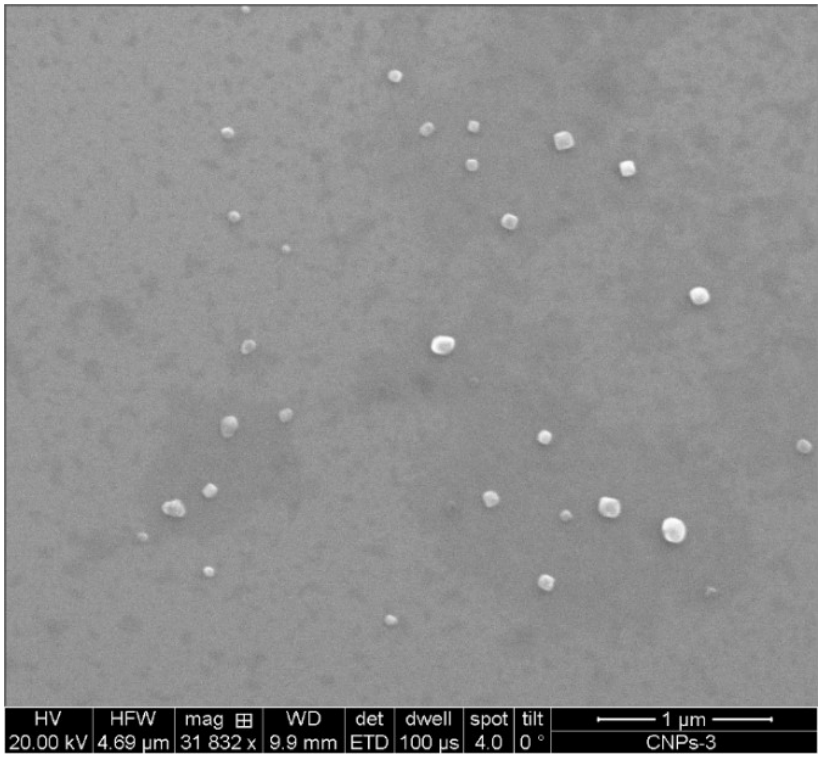

Figure 23: SEM Image of CNPs-3 with Particle Sizes between 50-200 nm.

3.2.2 Light Scattering Size Determination. Since the diameters of the CNPs-3 were quite small and approaching the limits of the SEM and this author's ability to resolve these particles, a Malvern NanoSight was used to affirm the sizing data obtained by using ImageJ. The NanoSight is a remarkable instrument which uses scattered light to size particles based on Brownian motion. The sample is placed in a small cell, where it is then illuminated by a laser. This cell is placed on an optical microscope where the objective lenses are perpendicular to the incident beam. Light scattered from the particles enters the objective lens and travels to a camera, which is used as the detector. The information from the camera is sent to the computer where the NanoSight software tracks the particles' movement. Since the volume of the cell is known, the software can then count the number of particles and determine concentrations of each particle size.

Figure 24 shows the results of the NanoSight experiment. The shape of the size distribution was not very similar to the results obtained using ImageJ. The results shown in this Figure are the average of five runs. Three of these runs showed significant concentrations of particles at low diameters, which can be seen in Figure 24 in the 0 to 36 nm region. The diameters with the highest concentration were between 72 and 150 nm. It also showed the "trail off" of the size distribution toward larger diameters like the ImageJ results. The size distribution was much wider for the NanoSight results than for the ImageJ. These larger particles may be aggregates.

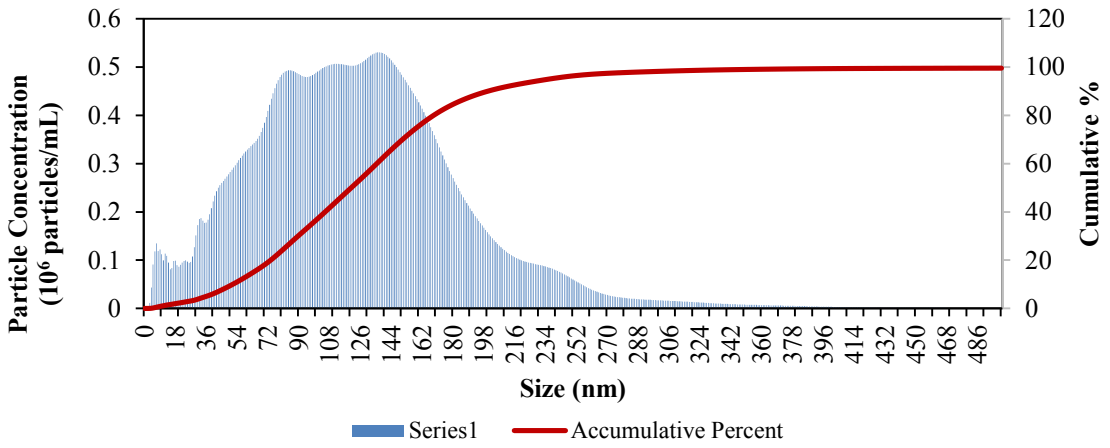

Figure 24: CNP-3 Size Distribution Obtained using a Light Scattering Technique. Data obtained using a NanoSight LM10 instrument.

3.3.0 Ultraviolet-Visible Spectroscopy

Ultraviolet-visible (UV-Vis) spectroscopy is a measurement of the amount of light a substance absorbs. Light is passed through the sample and on to a monochromator that splits the light up into small ranges of wavelengths by diffraction. The monochromator is then moved to shine these ranges one at a time onto the detector. A

spectrum is then obtained by measuring all the small ranges and combining them together.

The UV-Vis spectra of the CNPs were virtually identical between the three synthesis methods. Figure 25 shows that absorbance above 550 nm was very low, but below 550 nm the absorbance quickly increases and continues to increase all the way to 250 nm. Since it absorbed more strongly in the ultraviolet and blue region, the appearance of low concentration solution were yellow or amber.

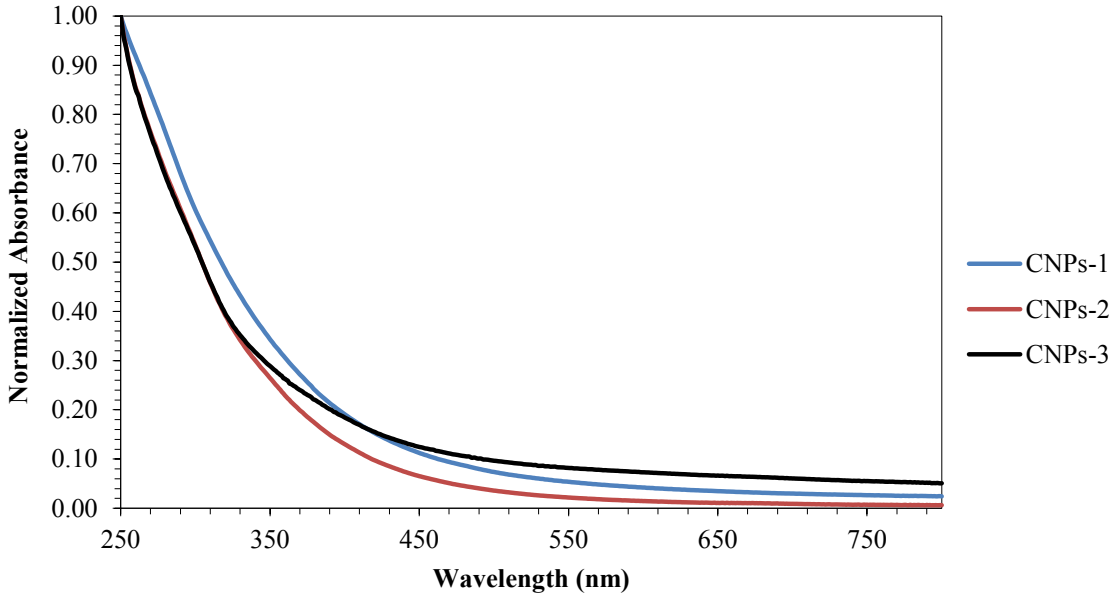

Figure 25: UV-Vis Spectra of CNPs-1, CNPs-2, and CNPs-3. All spectra were collected in dilute sodium hydroxide solution.

The absorbance spectra, of particles from the three methods, were very similar to those in the literature for carbon nanoparticles. All spectra in the literature have a similar shape, but a few reports have shown peaks on the gradual slope leading to 250 nm (see Figure 26).

3.4.0 Fluorescence Spectroscopy.

Fluorescence spectroscopy measures the radiative properties of materials. First, the sample is excited by an incident beam of light at a wavelength of your choosing. The wavelength chosen is sample dependent, but is related to the absorption spectrum. During excitation the electrons absorb energy and jump to a higher energy state.[58] In fluorescence the electron almost immediately returns to the ground state and the energy that was absorbed must be released.[58] There are non-radiative and radiative means by which this can occur, but since we are talking about fluorescence, a radiative process, then the energy is released as a photon. Each energy level also contains many vibrational sub-levels, so the photon released may have equal energy or less energy than the incident beam depending on which vibrational mode it returns to.[58] Since this is based on probability, when a sample is excited, multiple wavelengths are emitted with the peak intensity being the most probable transition.[58] These multiple wavelengths result in a spectrum of light that is recorded by the instrument's detector.

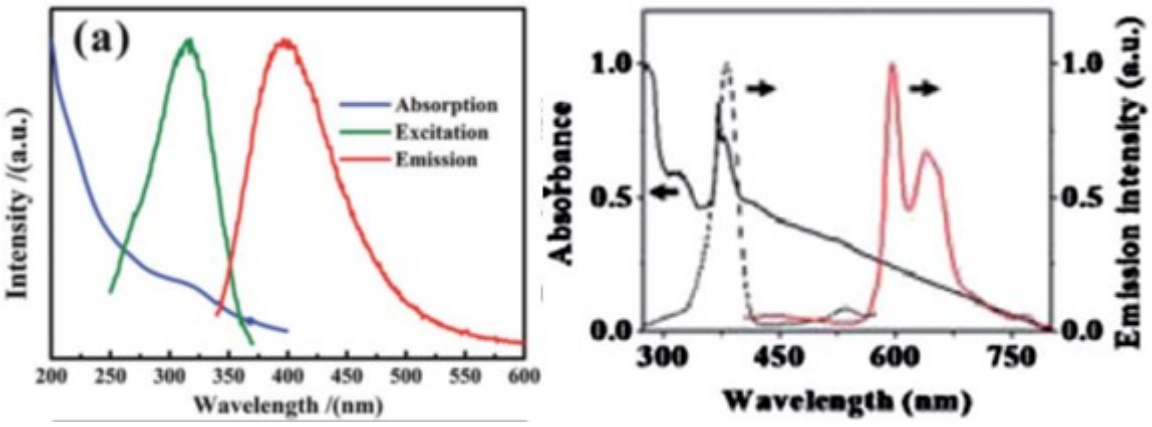

Figure 26: Example CNP UV-Vis and Fluorescence Spectra from Literature. Cdots were obtained by heating an aerosolized carbon sources (left) and by heating a mixture of a carbohydrate and H_3PO_4 (right).[13, 39]

The instrument has a monochromator that aligns the different emitted wavelengths onto the detector by diffraction.[59] This allows a very narrow range of wavelengths to hit the detector. As the monochromator is moved by the software, a wide range of wavelengths can be measured resulting in a spectrum.

The fluorescence spectra of the CNPs, made from the three methods, were virtually identical (see Figure 27). In a sodium hydroxide solution with pH above 9, the peak fluorescence is usually around 450-480 nm. This depends on several factors that include: pH, concentration, and excitation wavelength. The width of the peak is very broad spanning from around 380 to 700 nm. The fluorescence is very weak at 700 nm, but can still be measured.

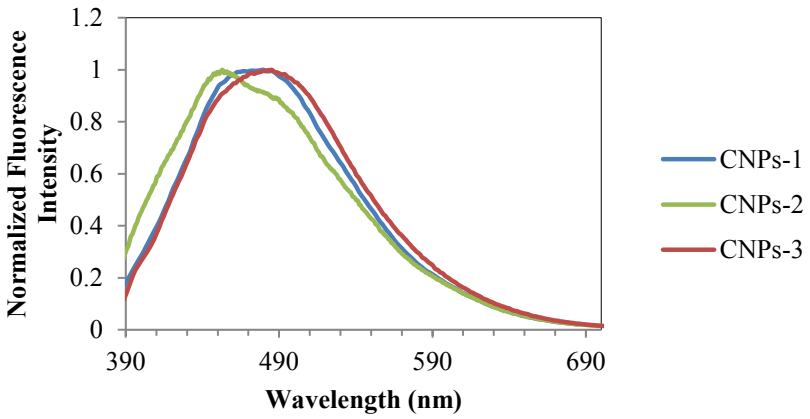

Figure 27: Fluorescence Spectra of CNPs-1, CNPs-2, and CNPs-3. Data collected with the excitation wavelength at 375 nm.

The effect of pH on the fluorescence spectrum is shown in Figure 28. It can be seen that at lower pH the peak emission shifts to lower energy wavelengths. A clear difference can be observed in the apparent color of solution while being excited. At pH 10 the observed color of the fluorescence is blue-green, while at a pH of 3 the

fluorescence is yellow-orange. The intensity of the fluorescence was reduced dramatically by lowering the pH as well. It is possible that surface functional groups may extend into the solution for a good solvent (pH 10) and recoil toward the particle surface in a poor solvent (pH 3). This recoil action may quench the fluorescence at lower wavelengths. This trend extends to other good solvents as well; the fluorescence appears green-blue in methanol, acetone, or ethyl acetate when the particles are in the protonated form.

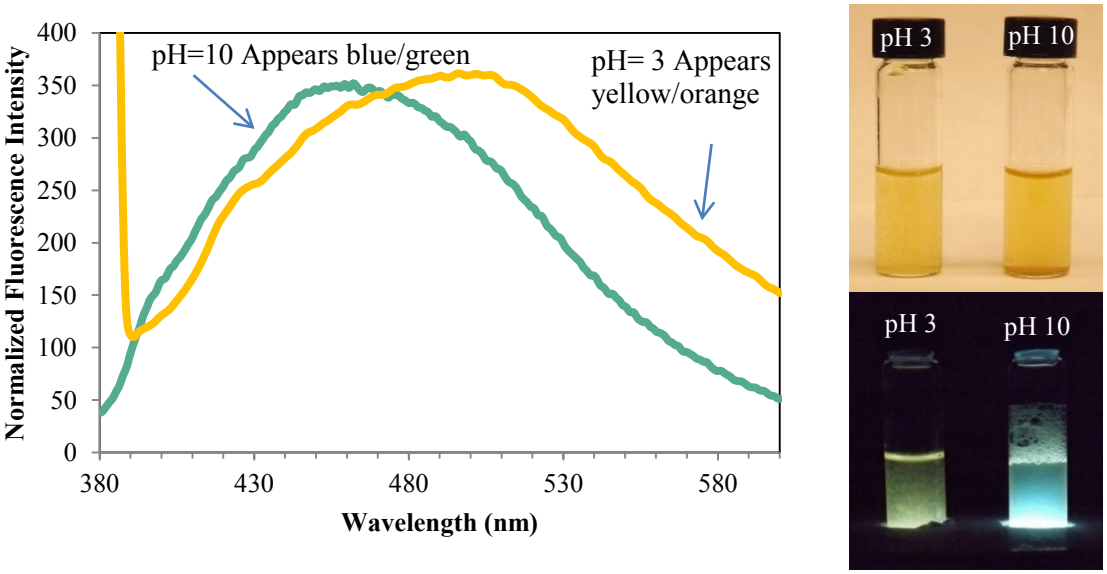

Figure 28: The Effect of pH on the Fluorescence of CNPs. The images show the appearance of the CNPs-3 at pH 3 and pH 10 under 365 nm UV light (bottom right) and white light (top right). The fluorescence spectra of CNPs-2 (left) at pH 3 and pH 10 with excitation wavelength at 375 nm, is also shown.

In the literature surrounding carbon nanoparticles or carbon quantum dots there is a common description of their fluorescence as being tunable (see Figure 29).[6-9] This arises from the broad emission spectrum. The apparent color or peak fluorescence can be chosen simply by changing the excitation wavelength. As the excitation wavelength is

shifted toward higher wavelengths the emission can be truncated (see Figure 30). Practical use of this tuned fluorescence may be limited at higher wavelengths due to lower quantum yield.

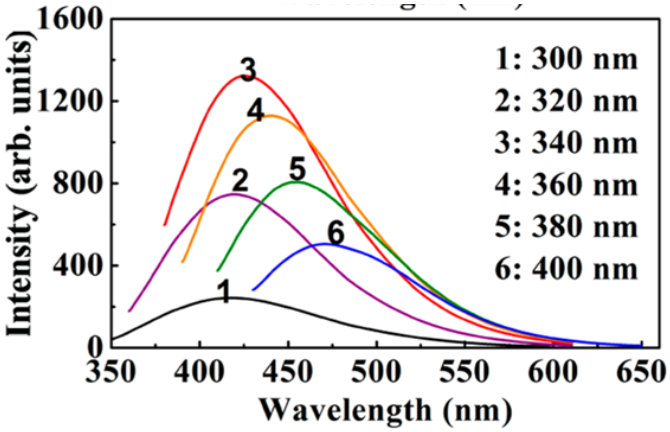

Figure 29: Literature Example of the Effect of Excitation Wavelength on the Fluorescence Spectrum of CNPs.[30]

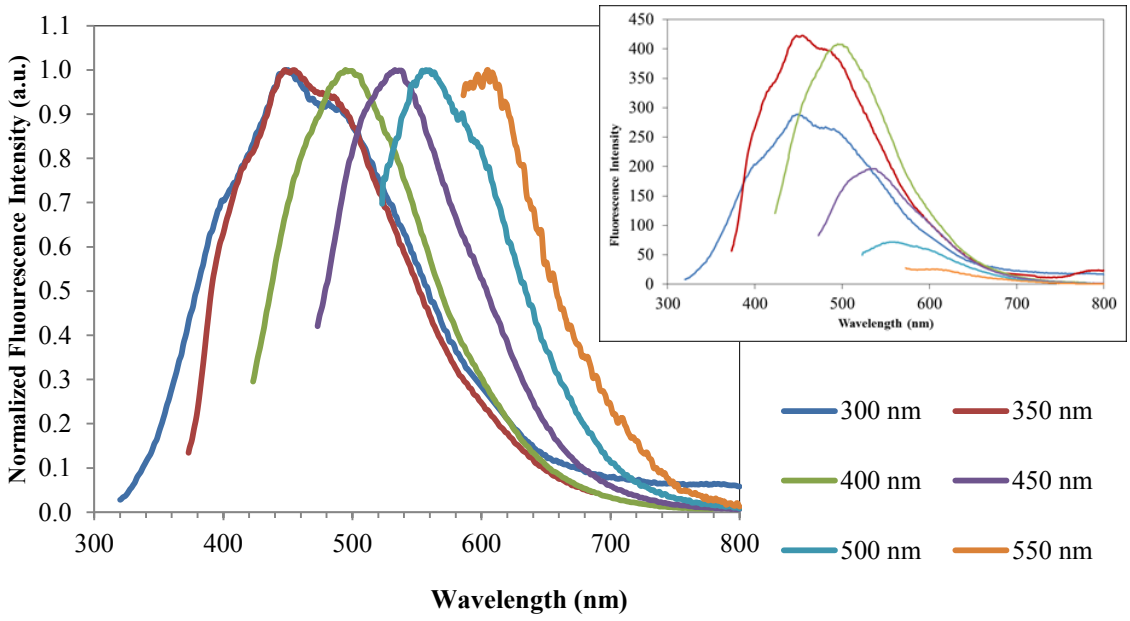

Figure 30: Fluorescence Spectra of CNPs-1 with changing Excitation Wavelengths. The main graph is normalized while the inset graph shows the spectra at their original intensities.

A similar effect could be seen when the concentration of the CNPs was increased.[8] There was a clear shift in both the apparent color toward higher wavelengths and in the intensity when the concentration was increased. This can be seen in Figures 31 and 32.

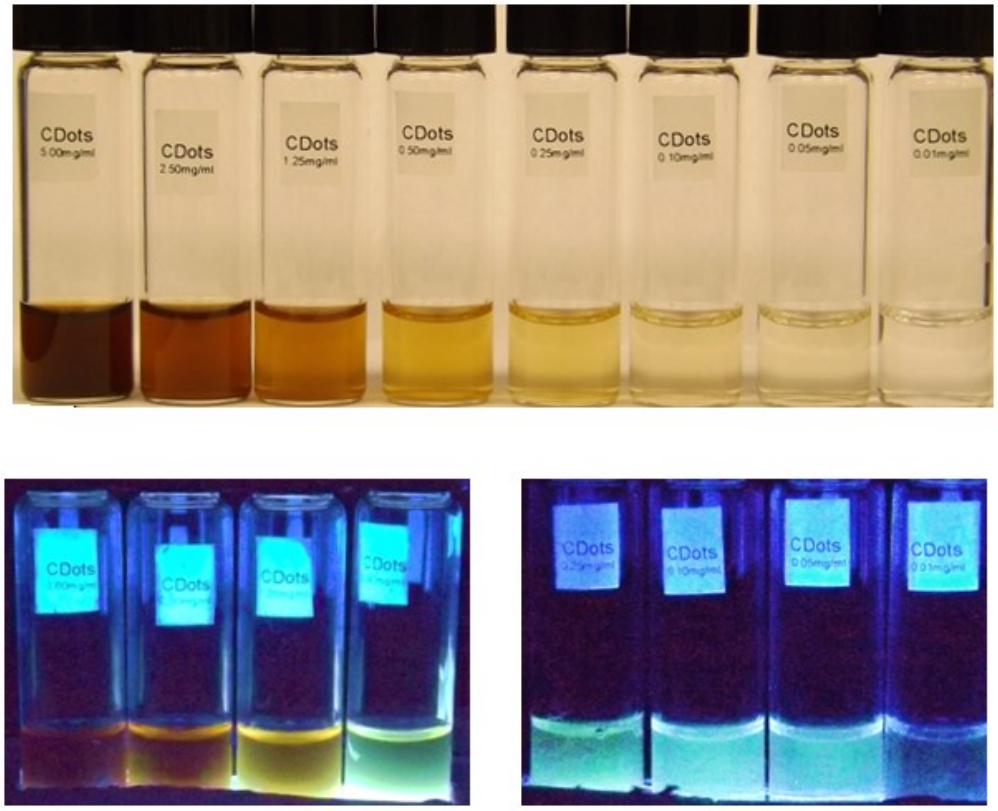

Figure 31: Picture showing the Effect of Concentration on the Fluorescence of CNPs. Top picture shows solutions of CNPs under white light and the bottom pictures shows the same solutions under 365 nm UV light. The concentrations, from left to right, were: 5.00, 2.50, 1.25, 0.50, 0.25, 0.10, 0.05, and 0.01 mg/mL.

The fluorescence increases initially with increasing concentration, but the wavelength where the maximum fluorescence occurs, does not change significantly (see Figure 32 and Table 2). The maximum intensity occurred around 0.10 mg/mL of CNPs

and the peak was around 290 nm (see Table 2). The fluorescence intensity began to decrease again when the peak began to shift toward the higher wavelengths. It is believed that this shift was due to absorption of the lower wavelength emissions by the other particles in the solution. As seen in Section 3.3.0, the CNPs absorb light more strongly at lower wavelengths, which would allow more of the longer wavelength light to escape the solution. As the concentration increased the apparent color of the solution (under white light) went from clear to yellow, then amber, then reddish brown, and finally brown (see Figure 31).

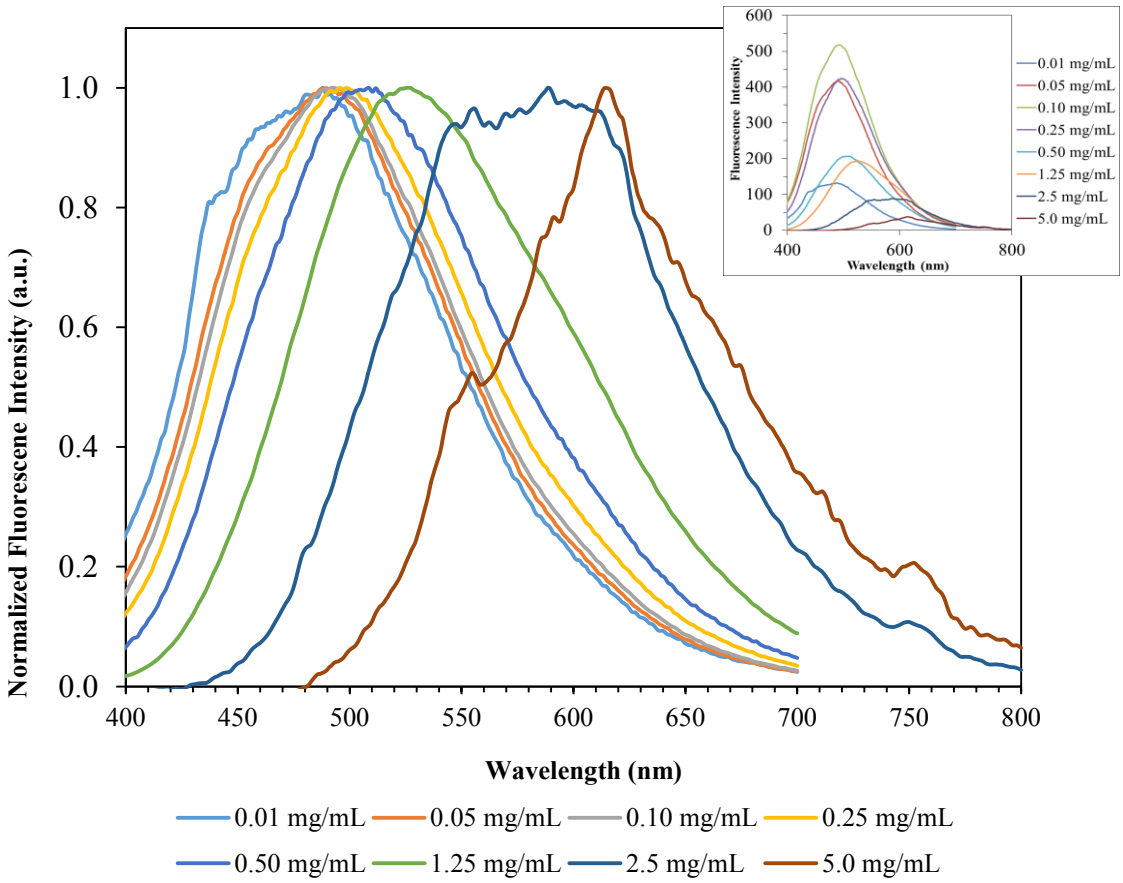

Figure 32: Effect of Concentration on the Fluorescence Spectrum of CNPs. The excitation wavelength was 375 nm. The main graph is normalized while the inset graph is at the original intensities.

Table 2: The Effect of CNP Concentration on Peak Fluorescence Wavelength and Intensity.

Concentration (mg/mL)	Peak Fluorescence Wavelength (nm)	Fluorescence Intensity
0.01	488	132.50
0.05	492	416.85
0.10	493	518.00
0.25	499	424.06
0.50	508	207.21
1.25	526	193.42
2.50	581	89.196
5.00	614	37.757

CHAPTER 4: SQUARE WAVE VOLTAMETRIC DETECTION OF METAL CATIONS IN AQUEOUS SOLUTION USING CARBON NANOPARTICLE MODIFIED GLASSY CARBON ELECTRODES

4.1.0 Square Wave Voltammetry

The application chosen for the CNPs was the electrochemical detection of heavy metals. This was chosen because electrochemical techniques offer low detection limits, differentiation between metals, and reliability. All of these attributes are important for real world use of this application.

Heavy metal detection is vital to safe drinking water. The Environmental Protection Agency regulates the amount of many heavy metals in drinking water. The current Maximum Contaminant Limits for mercury, lead, and copper are: 2 ppb, 13 ppb, and 1.3 ppm, respectively.[57] Ideally, the limits for mercury and lead would be zero, but they are limited by technology. Current technologies limit the reliable detection of concentrations lower than this.

In Chapter 1 it was discussed how in literature many groups have demonstrated that heavy metals can be detected using CNPs or Cdots through the metal's ability to quench fluorescence. Duplication of this was tried with the CNPs, however the selectivity was poor, which resulted in quenching of the fluorescence by many metals (see Figure 33). This problem was easily overcome by the nature of electrochemical techniques. The potential at which metals are oxidized is fairly unique (see Figure 34).

Square wave voltammetry (SWV) was chosen as the detection method for metal ions for a few reasons. The main reason being that SWV has very low detection limits.

These limits are often in the 10^{-8} M region.[59] It is a high amplitude pulsed technique that allows for both forward (oxidation) and reverse (reduction) scans to be collected simultaneously. By combining these two scans it allows for an increase in peak current, which increases the ability to detect low concentrations.

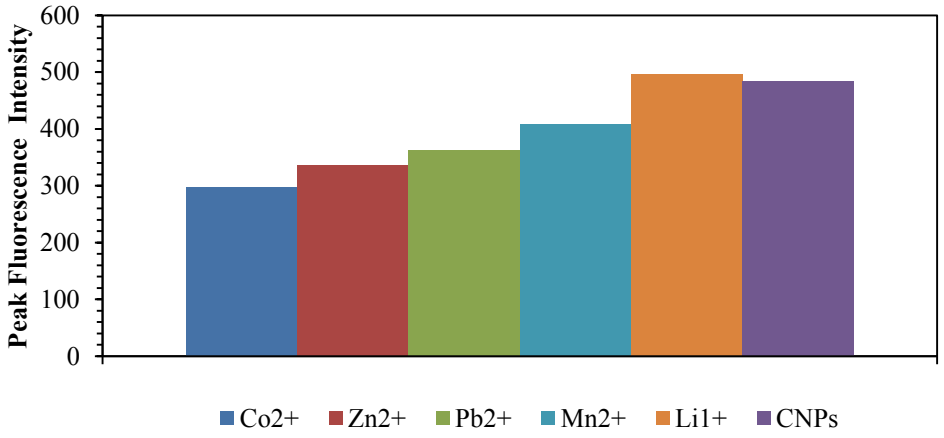

Figure 33: CNP Fluorescence with Metal Ions in Aqueous Solution. Solutions containing 0.3 mg/mL of CNPs were prepared containing 1.4 mM Li^{1+}, 1.0 mM Co^{2+}, 2.5 mM Zn^{2+}, 1.3 mM Pb^{2+}

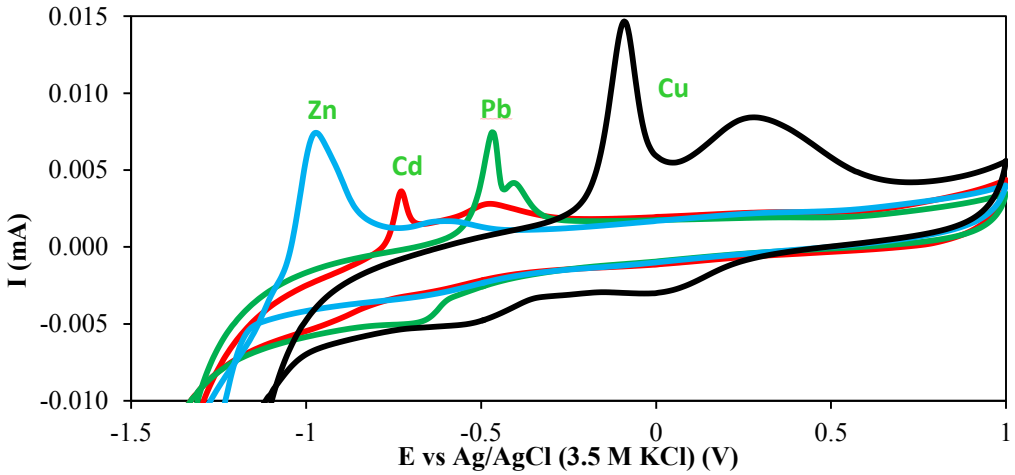

Figure 34: Cyclic Voltammograms of Zinc, Cadmium, Lead, and Copper. Obtain using a CNP-2 modified GCE accumulated in 0.10 M CH_3COONa solution containing 100 ppm of the divalent metal ion.

The square wave part of SWV refers to the applied potential at the working electrode. This is a "pulsed" technique where the potential is increased by a specific amount for a few milliseconds and then is decreased by an equal amount below the starting potential for the same amount of time (see Figure 35). The square wave is then superimposed over a staircase. The staircase is a stepwise increase in the midpoint potential of the square wave. The pulse height (PH) is the size of the square wave, pulse width (PW) is the time duration of the square wave pulse, and step height (SH) is the increase in the midpoint potential of the square wave over time (see Figure 36).

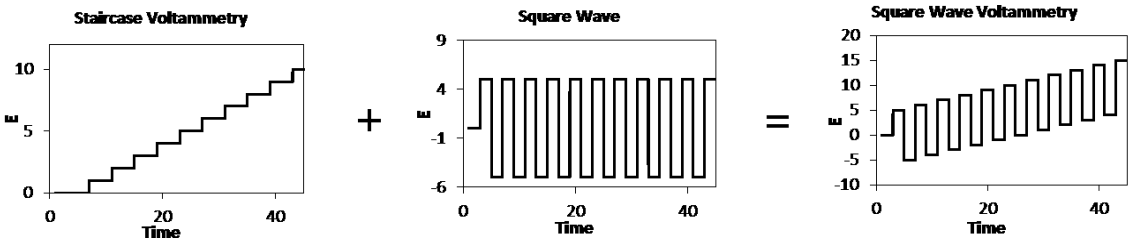

Figure 35: Diagram of Square Wave Voltammetry.

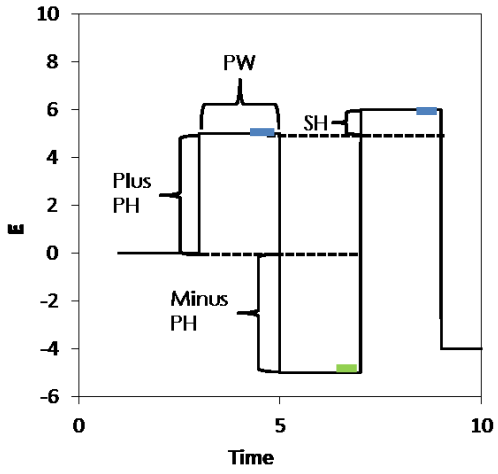

Figure 36: Diagram Defining the Parameters of Square Wave Voltammetry. Blue squares denote the section of the pulse where the $I_{forward}$ is collected and the green square denotes where the $I_{reverse}$ is collected.

The direction that the potential is scanned determines the type of SWV is performed. Let us say that left is toward negative potential values and right is toward positive potential values. With this in mind, then square wave anodic stripping voltammetry scans to the right and square wave cathodic stripping voltammetry scans to the left. Anodic stripping was performed, so the potential was scanned from negative potential values to positive potential values or to the right. The choice of anodic versus cathodic stripping is determined by the analyte studied.

The oscillation of the potential allows for oxidation and reduction to occur. During the plus pulse (see Figure 36) oxidation happens and during the minus pulse reduction happens. Since the potential quickly switches back and forth between the plus and minus pulses, any electroactive species present are oxidized then quickly reduced. This produces two simultaneous scans. The current collected at the end of the plus pulses is denoted as the forward scan and the current collected at the end of the minus pulses is denoted as the reverse scan. To take advantage of the forward and reverse scans, they are combined into a single data set (ΔI), as shown in Equation 4.1. That is, the reverse scan is subtracted from the forward scan:

$$\Delta I = I_{\text{forward}} - I_{\text{reverse}} \qquad \text{Equation 4.1}$$

and for a completely reversible system,

$$I_{\text{forward}} = -I_{\text{reverse}}$$

$$\Delta I = 2I_{\text{forward}} \qquad \text{Equation 4.2}$$

therefore, the combined peak current (ΔI_{peak}) is larger than the peak current of the forward scan alone for any system that is at least partially reversible (see Figure 37). Figure 37 shows how the forward and reverse scans are nearly mirror images of each other. Since

the current flows in opposite directions for the forward and reverse scans, the forward scan current is positive and the reverse scan current is negative.

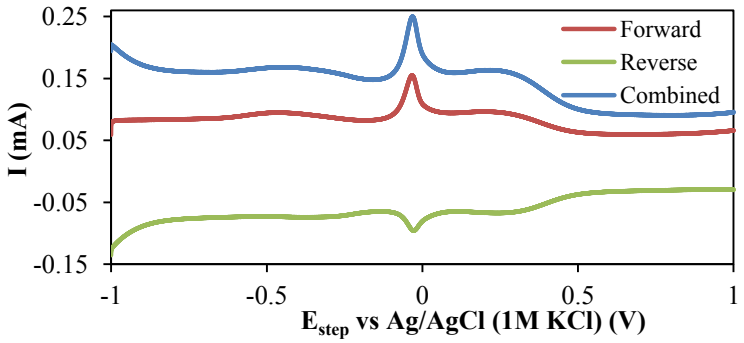

Figure 37: SWV with the Forward and Reverse Scan Components. Collected using a CNP-3 modified GCE accumulated in 100 ppm Cu^{2+} in 1.0 M CH_3COONa.

4.1.1 Measuring Peak Currents in Voltammetry. There are several methods for measuring peak currents (ΔI_{peak}) in voltammetry. The main issue with measuring peak currents is: the background current in voltammograms often varies significantly from run to run. This makes absolute peak height measurements, as measured from zero, have large coefficients of variation and would hinder low detection limits. The most common method to overcome this variance, is to draw a line from the linear portion of the background just before the peak and measure the distance from the peak to this line (see Figure 38). This method is well suited for linear backgrounds or when there is at least a portion that is linear just before the peak. This method was used throughout this research except in the case of the final copper calibration curve.

Another common method used to measure peak currents, is to draw a line from the background on one side of the peak to the background on the other side of the peak. Then the peak current is measured from this line to the top of the peak (see Figure 39).

This technique is good when the background has limited linear nature before the analyte peak. This method was chosen for the final copper calibration curve. The EC-Lab software has both of these methods built into it and this was taken advantage for measuring the peak currents (see Section 4.2.2).

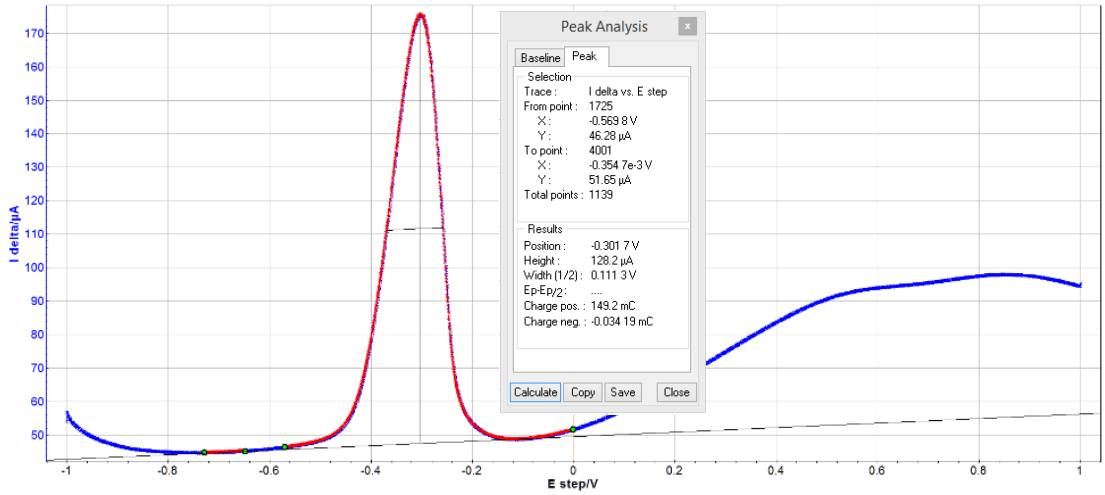

Figure 38: Measuring Peak Current with Linear Background. Obtained using EC-Lab software.

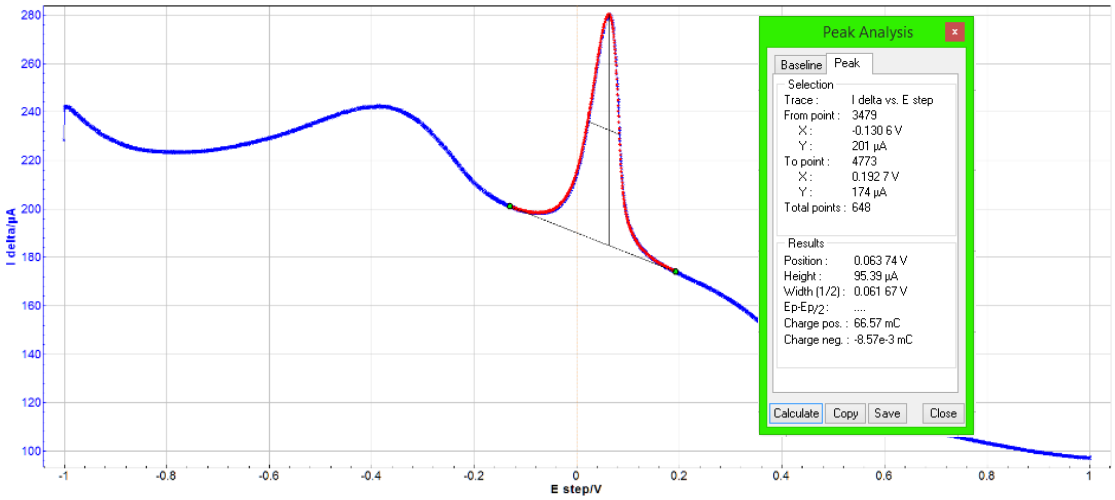

Figure 39: Measuring Peak Current with Non-Linear Background. Obtained using EC-Lab software.

4.1.2 Calculation of Low Detection Limits from Calibration Curve. The method chosen to calculate low detection limits was based on the linear regression of the calibration curve. This method was chosen because of its simplicity. To perform this method the calibration curve must be blank corrected, linear, and 7 or more runs must be performed with a concentration 1-5 times the low detection limit.[61] Using this method, the low detection limit peak current (ΔI_{LDL}) is defined as:

$$\Delta I_{LDL} = \Delta\overline{I}_{blank} + 3S_{\Delta I_{peak}} \qquad \text{Equation 4.3}$$

and for a linear calibration curve the regression line should be of the form $y = mx + b$, therefore

$$\Delta\overline{I}_{peak} = m[M] + \Delta\overline{I}_{blank} \qquad \text{Equation 4.4}$$

where $\Delta\overline{I}_{peak}$ is the average peak current for 7 or more replicates of concentration 1-5 times the low detection limit, m is the slope of the calibration curve, [M] is the concentration of the metal analyte, $S_{\Delta I_{peak}}$ is the standard deviation of the peak current for the 7 or more replicates, and $\Delta\overline{I}_{blank}$ is the average blank peak current. Since the low detection limit is the concentration of analyte that gives a signal significantly different from the blank,

$$[M] = \text{Low Detection Limit} \qquad \text{Equation 4.5}$$

and

$$\Delta\overline{I}_{peak} = \Delta I_{LDL} \qquad \text{Equation 4.6}$$

upon substitution and rearrangement Equation 4.4 reduces to:

$$\text{Low Detection Limit} = 3S_{\Delta I_{peak}}/m \qquad \text{Equation 4.7}$$

4.2.0 Optimization of SWV Parameters

There are many steps in the process of SWV. These steps needed to be optimized for the system being studied. In this section optimization of many of the steps seen in Figure 40 will be discussed. Also, you will be taken through the process which leads to each metal requiring unique parameters. While some of the parameters could be carried over from one metal to the next, some were not. The parameters that could be carried over will be discussed first and those that are unique to the individual metals will be discussed separately.

There are several goals that can be chosen for optimization. It was chosen to optimize for reproducibility initially by selecting for conditions that gave the lowest coefficient of variation. However, this did not always prove to be the best for sensitivity, which shall be define as the slope of the calibration curve or how sensitive the ΔI_{peak} is to changes in analyte concentration.

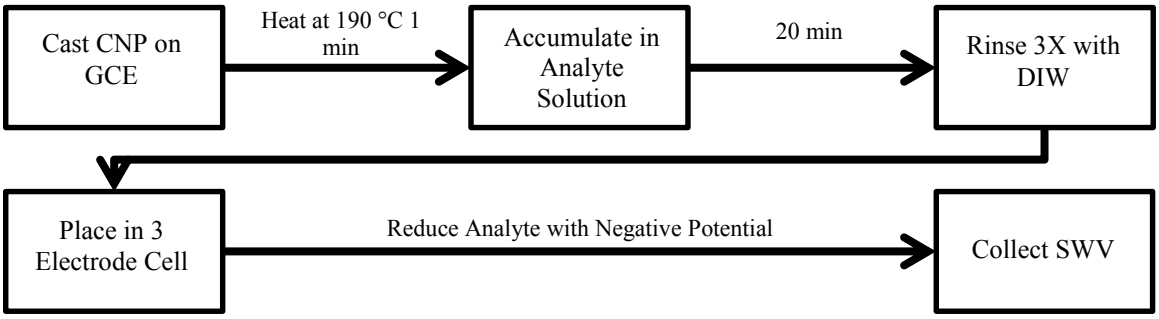

Figure 40: Overview of SWV Method.

4.2.1 Accumulation. The time the electrode spent in the analyte solution is known as the accumulation time. This time was optimized by suspending a CNP-2 modified GCE in 100 ppm Pb^{2+} in 0.10 M CH_3COONa solution for various amounts of

time. Then cyclic voltammetry was performed and the peak currents were compared. This parameter was used for all metals.

It can be seen in Figure 41 that the peak current increased with increased time in the analyte solution up to 15 min. Beyond this point the peak current no longer showed this trend. It should be noted that at the time of this study, casting had not been optimized and reproducibility was low. With this in mind, it was decided that a 20 min accumulation time would be sufficient.

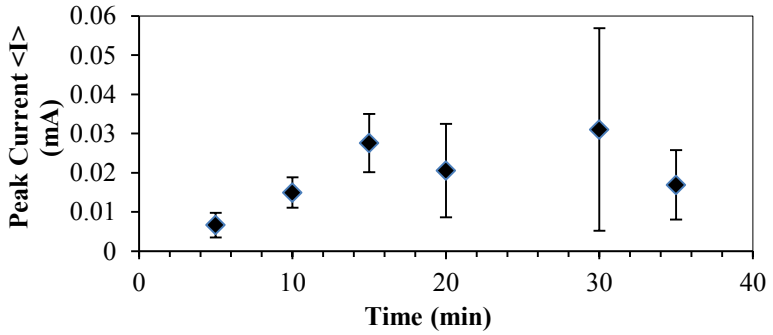

Figure 41: Accumulation Time Study. Obtained by accumulation in a 100 ppm Pb^{2+} in 0.1 M CH_3COONa and performing cyclic voltammetry. Error bars are at the 95% confidence level.

4.2.2 Software SWV Parameters. The software used to control the potentiostat for the SWV was EC-Lab version 9.41 by Bio-Logic Science Instruments. For SWV this software allows you to choose several parameters. These include: PH, SH, PW, reduction potential, reduction time, scan ending potential, percent of each step to average current, and current range. PH, SH, and PW were discussed earlier in this chapter. The reduction potential is the voltage applied to the working electrode to reduce the analyte prior to SWV and the reduction time is the amount of time this voltage is applied. The

percent of each step to average current determines how much time the current is averaged for each pulse. The current is averaged over the end of the pulse to eliminated capacitive currents, so that only Faradaic currents are recorded. Generally, only a few milliseconds at the end of each step are recorded, which improves sensitivity. The current range is chosen based on the expected maximum current observed in the voltammogram. It is used to set the proper internal resistance of the potentiostat. The PW, PH, SH, and the reduction time were optimized. The reduction potential was chosen based on the limits of the platinum wire counter electrode, which begins to oxidize at potentials below -1.0 V.

The reduction time was optimized by suspending a CNP-3 modified GCE in a 100 ppm Cu^{2+} in 0.10 M CH_3COONa solution for 20 min and then applying a reduction potential of -1.0 V for various amounts of time. Figure 42 shows the results of this study. In general, with increasing reduction time, the ΔI also increased. From this data, a reduction time of 5 min was chosen. This was chosen because it gave the largest ΔI and testing beyond the 5 min reduction time did not occur in order to minimize the overall experiment time. It is possible that better sensitivity could be achieved with a longer reduction time.

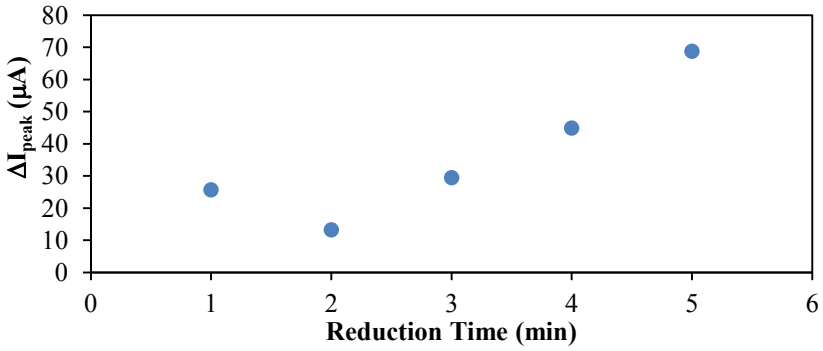

Figure 42: Optimization of Reduction Time. Obtained by accumulation in a 100 ppm Cu^{2+} in 0.1 M CH_3COONa and performing SWV.

The optimization of the PH was carried out using a 100 ppm Pb^{2+} analyte in 1.0 M CH_3COONa solution. The CNP-3 modified GCEs were accumulated in this solution for 20 min and SWV was performed with various PH values. From Figure 43 it can be seen that the PH has a significant impact on ΔI_{peak} from 100 to 200 mA where there was about a 10 times increase between those two settings. With PH settings above 200 mA, it can be said that there was not an increase in ΔI_{peak}, therefore 200 mA was chosen for the PH. Also, as the PH increased the position of the peak shifted toward more negative potentials and the background current became more skewed (see Figure 44). At 100 mA the background was quite flat compared to the background at 500 mA, which was very much "U" shaped. The shape of the background has a significant impact on measuring ΔI_{peak}.

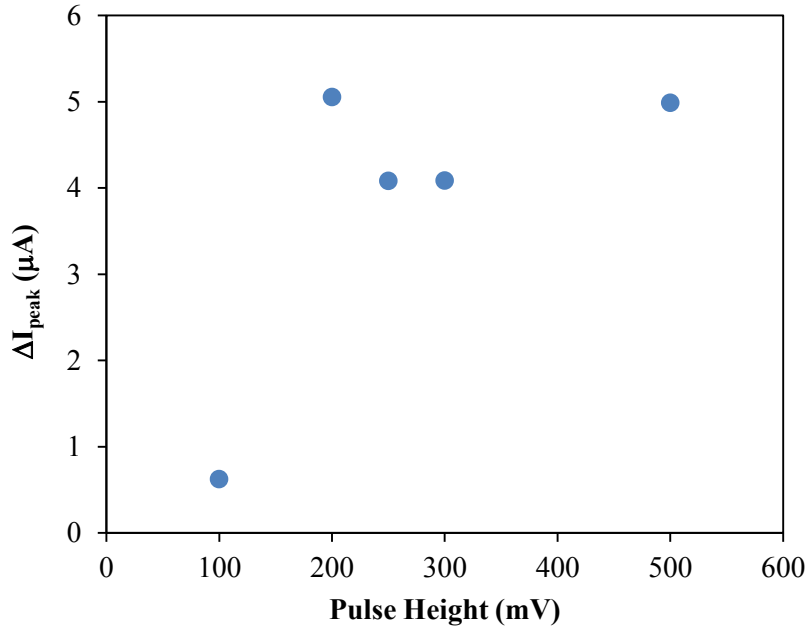

Figure 43: Optimization of Pulse Height. Obtained by accumulation in a 100 ppm Pb^{2+} in 1.0 M CH_3COONa and performing SWV.

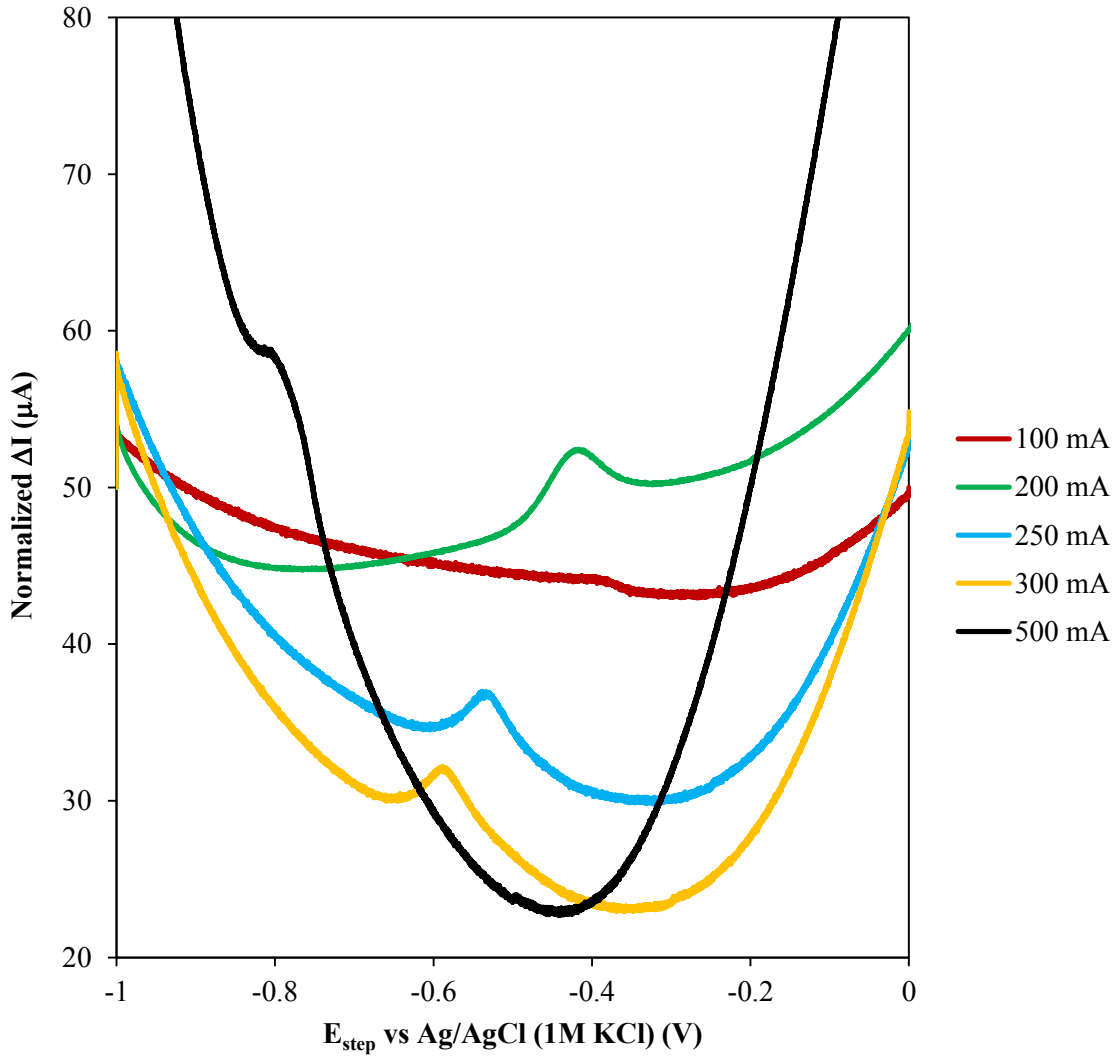

Figure 44: Optimization of Pulse Height Square Wave Voltammograms. Obtained by accumulation in a 100 ppm Pb^{2+} in 1.0 M CH_3COONa and performing SWV.

The PW was optimized by suspending a CNP-3 modified GCE in a 10 ppm Pb^{2+} in 1.0 M CH_3COONa solution and performing SWV at various PW settings. The results of the study are shown in Figures 45 and 46. The general trend: decreasing the PW resulted in higher ΔI_{peak} while broadening the peak. Also, a significant amount of "lean" was noticed at smaller PWs. It was felt that this lean may have a significant impact on measuring ΔI_{peak} and therefore 2.4 ms was chosen for the PW.

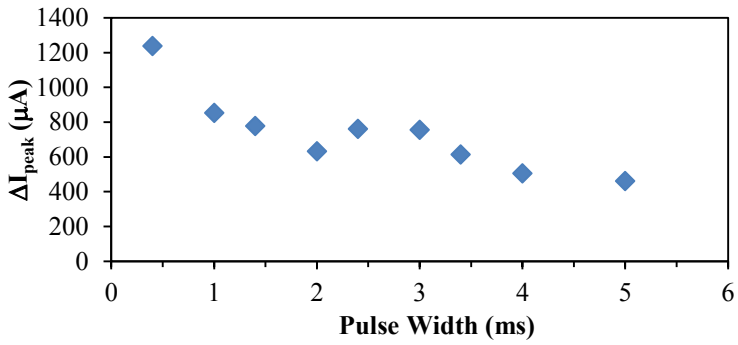

Figure 45: Optimization of Pulse Width. Obtained by suspending CNP-3 modified GCEs in a 10 ppm Pb^{2+} in 1.0 M CH_3COONa and performing SWV.

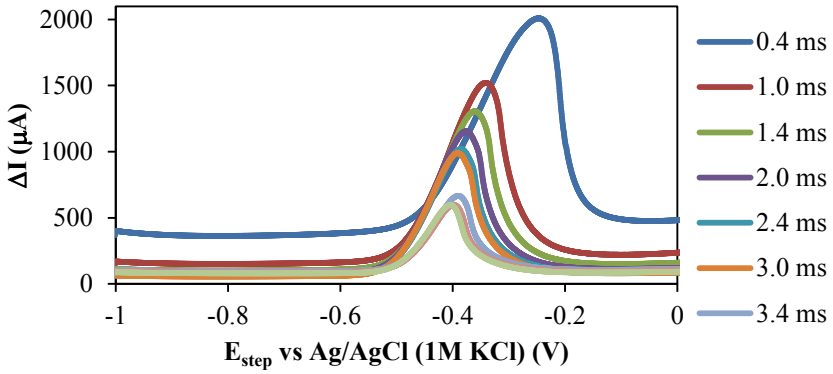

Figure 46: Optimization of Pulse Width Square Wave Voltammograms. Obtained by suspending CNP-3 modified GCEs in a 10 ppm Pb^{2+} in 1.0 M CH_3COONa and performing SWV.

4.2.3 CNP Modified GCE Preparation. The preparation of the CNP modified GCEs was very challenging. They were prepared by drop casting the CNPs from a suspension and allowing them to dry. The CNPs had a tendency to fall off the GCE once placed in the analyte solution. As one can imagine, this caused significant issues with reproducibility. Many attempts were made to find something that would bind the CNPs to the GCE with little success. After months of work, a very simple solution was found. The answer was to heat treat the castings.

Heating the CNPs above 170° C causes them to melt or dissolve. As discussed in Chapter 3, the CNPs seem to retain solvent. Once heated, this solvent begins to boil out of the CNPs, but just before that occurs the CNPs change from a light brown powder to a dark brown viscous liquid. When cooled the CNP solidify into a hard, dark brown continuous solid. This solid can then be ground back into a light brown powder. A similar result can be obtained by dissolving the CNPs in a good solvent, such as methanol or acetone, and then drying them. Heating the CNP castings for a limited time allows for them to partially melt, which prevents them from falling off when placed in the analyte solution.

This phenomenon is shown in Figure 47. After heating for 0.5 min there was no visible change in CNPs. At 1.0 min the edges of the castings became darker brown while the center remained close to the original color. After 1.5 min the centers of some castings were noticeably darker brown. Beyond that the casting fully melt and turn very dark brown.

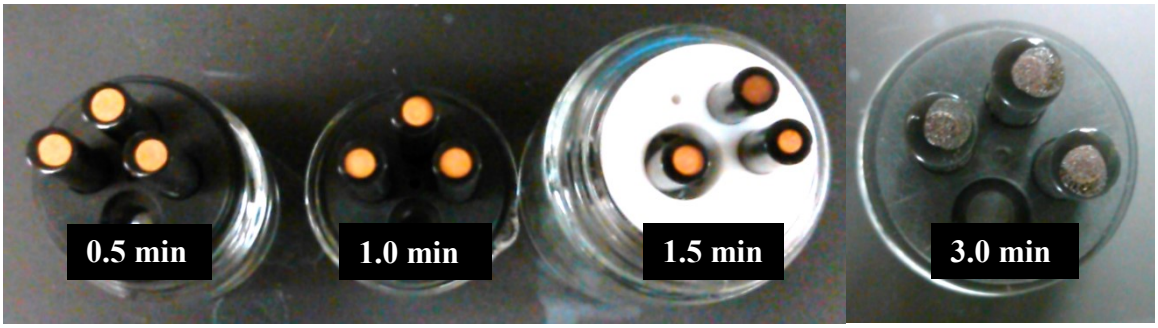

Figure 47: Image of CNP-3 Modified GCEs after Heat Treatment.

To determine the amount of heat treatment time needed to stabilize the CNP castings, CNP-3 modified GCE electrodes were prepared. Then they were heat treated

for various amounts of time in a 190° C oven. These electrodes were then accumulated in a 100 ppm Cu^{2+} in 1.0 M CH_3COONa solution with the normal parameters discussed above and SWV was performed.

Figure 48 contains the results of the heat treatment study. Heating the CNP-3 castings up to 1 min did not result in any increase or decrease in ΔI_{peak}, but the variation of ΔI_{peak} between runs was impacted, which is demonstrated by the error bars. Beyond 1 min, the variance increased again and beyond 1.5 min the ΔI_{peak} began to decrease. This suggests that the best heat treatment time was 1 min and this time was used for all CNP-3 Castings.

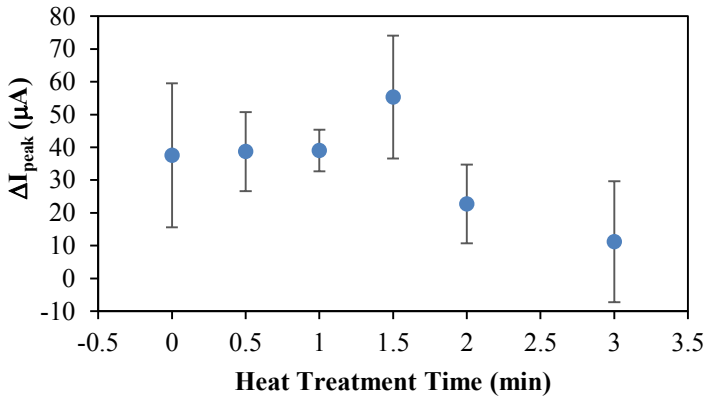

Figure 48: Heat Treatment Stabilization of CNP-3 Modified GCE Electrodes. The solution cast had a CNP-3 concentration of 26 mg/mL. The solution was cast in 10 μL increments and dried between each casting. The electrodes were accumulated in 100 ppm Cu^{2+} in 1.0 M CH_3COONa. Error bars are at the 95% confidence level.

4.2.4 Temperature Effect on Metal Detection. The temperature of the accumulation solution affects the ΔI_{peak} significantly. This can be seen in Figure 49. The

sensitivity of copper detection to temperature was 8.4 μA/°C. This data suggests that at elevated temperature the detection limits should be lower.

The temperature effect caused issues in collecting the calibration curves. Construction in the building caused wide temperature changes in the laboratory where these experiments were carried out. Reproducibility from one hour to the next or one day to the next was limited by the lack of temperature control.

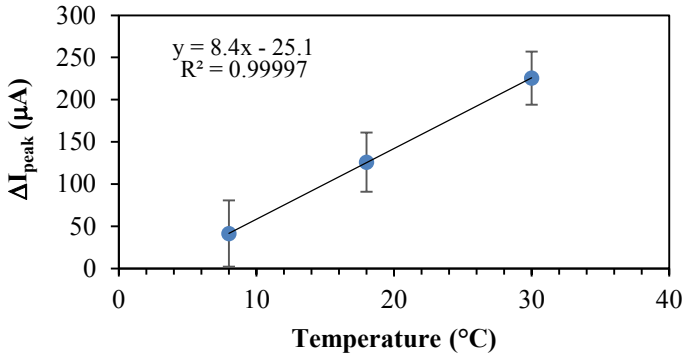

Figure 49: The Effect of Analyte Solution Temperature on Copper Detection with SWV. The temperature of the 100 ppm Cu^{2+} in 1.0 M CH_3COONa (pH 5.98) was controlled by placing it in a water bath containing either ice or warm water.

4.3.0 SWV Detection of Copper

In this section some parameters that were optimized specifically for copper and the calibration curves obtained will be discussed. These were the accumulation solution pH and electrode preparation. The progression of this research toward better sensitivity and, therefore, lower detection limits will be demonstrated.

4.3.1 CNP-3 Modified GCE Optimization for Copper Detection. The amount of CNPs-3 cast onto the GCEs was optimized for copper detection. This was completed by casting various amounts of CNPs-3 onto the GCE in 20 μL increments and drying in a

55 °C oven between castings. These electrodes were then accumulated in a 100 ppm Cu^{2+} in 1.0 M CH_3COONa solution.

Figure 50 shows how increasing the amount of CNPs-3 cast on the GCE changes the ΔI_{peak}. The variance between electrodes was fairly low up to the 0.78 mg cast, but increased dramatically at greater amounts cast. Above 1 mg cast the ΔI_{peak} was the highest and was nearly double that of the highest ΔI_{peak} below 1 mg. With the long battle fought over casting stability, a 0.5 mg cast was chosen for the initial calibration curves because it had the lowest variance with the highest ΔI_{peak}. For later calibration curves, a 1.0 mg cast was chosen to improve the sensitivity of the calibration curve and lower the detection limit (see Section 4.3.3).

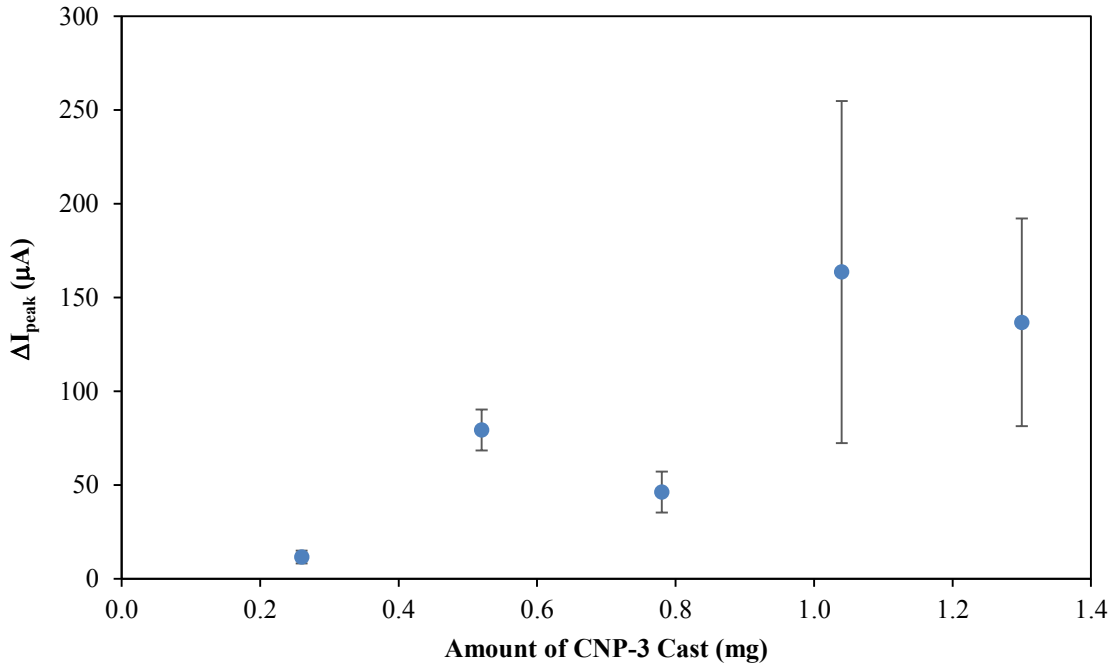

Figure 50: Optimization of CNP-3 Modified GCE Based on Amount of CNPs Cast. The solution cast had a CNP-3 concentration of 26 mg/mL. The solution was cast in 10 μL increments and dried between each casting. The electrodes were accumulated in 100 ppm Cu^{2+} in 1.0 M CH_3COONa. Error bars are at the 95% confidence level.

4.3.2 Accumulation pH Optimization for Copper Detection. It was determined early on that pH seemed to have an effect on the ΔI_{peak}. Evidence for this was seen in the preliminary test for copper detection. In this test $Cu(NO_3)_2$ in 2% HNO_3 was used to prepare a 100 ppm Cu^{2+} solution with pH ~ 1 for accumulation. This resulted in no peak being seen in the cyclic voltammogram. However, a peak was present when $Pb(NO_3)_2$ solid was used to prepare a 100 ppm Pb^{2+} accumulation solution with pH ~ 5. This lead us to try a 100 ppm Cu^{2+} in 0.10 M CH_3COONa accumulation solution made from the $Cu(NO_3)_2$ in 2% HNO_3 solution and a peak was obtained. From this, it was determined that the pH of the accumulation solution must be optimized.

To optimize the pH of the accumulation solution, several solutions containing 100 ppm Cu^{2+} were made from the $Cu(NO_3)_2$ in 2% HNO_3 solution at various pH values. CH_3COONa and CH_3COOH were used to control the pH of these solutions and two concentrations of the CH_3COOH/CH_3COONa buffer were used.

The results of this study were quite interesting. It became clear that pH did not have an effect on the ΔI_{peak}. Figure 51 shows that with increasing pH the ΔI_{peak} increases, but when the concentration of the CH_3COOH/CH_3COONa buffer is changed from 0.10 M to 1.0 M the ΔI_{peak} decreased and then began to increase again with increasing pH.

To determine the correlation between the buffer concentration and the ΔI_{peak}, the concentrations of both CH_3COOH and CH_3COO^- were calculated using the Henderson-Hasselbalch equation and the pH of the solutions. When the ΔI_{peak} was plotted versus these concentrations, it was determined that the concentration of the CH_3COOH had a significant impact on the ΔI_{peak}, while the concentration of the CH_3COO^- did not (see

Figure 52). This knowledge greatly influenced the sensitivity of the copper calibration curve (see Section 4.3.3).

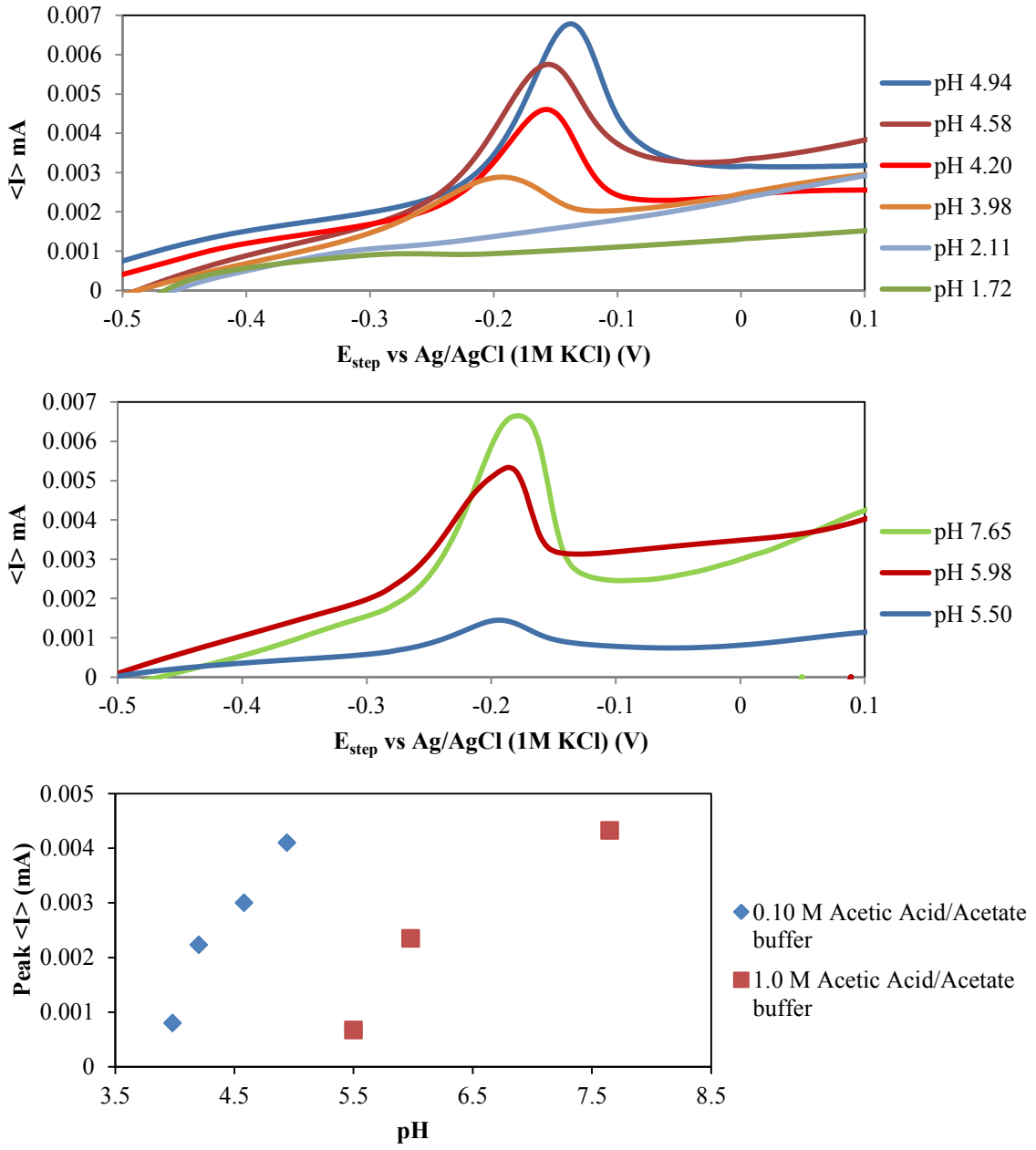

Figure 51: Analyte Solution pH Study. Cyclic voltammograms obtained by accumulation in a 100 ppm Cu^{2+} in 0.10 CH_3COONa buffer at several pH values (top), cyclic voltammograms obtained by accumulation in a 100 ppm Cu^{2+} in 1.0 CH_3COONa buffer at several pH values (middle), and peak current at these various pH values for both concentrations of the CH_3COOH/CH_3COONa buffer (bottom).

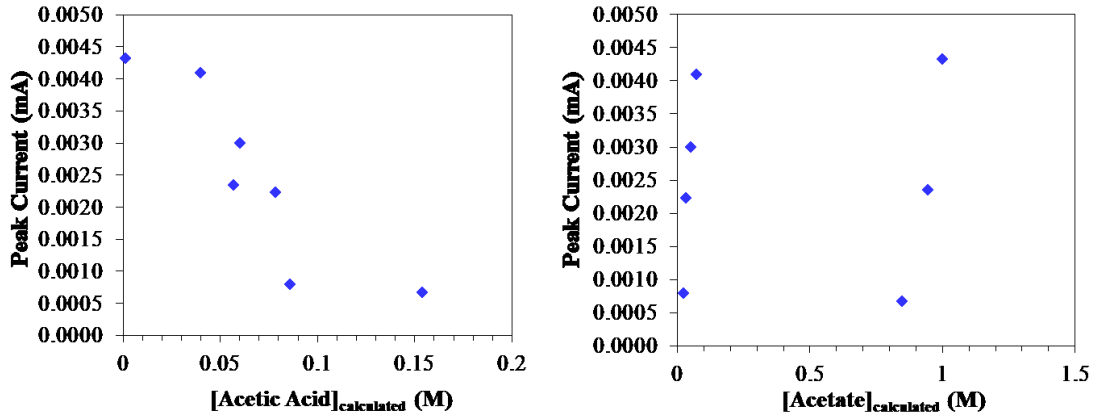

Figure 52: Analysis of the Analyte Solution pH Study. The peak current versus the calculated CH_3COOH concentration (left) and the CH_3COO^- concentration (right) from the cyclic voltammograms of the 100 ppm Cu^{2+} in both 0.1 M and 1.0 M CH_3COONa buffer.

4.3.3 Copper Calibration Curves. The first attempt at a calibration curve for copper gave results that are not acceptable. These data was collected using Cu^{2+} analyte solutions with 1.0 M CH_3COOH/CH_3COONa buffer with a pH of 5.98. The calibration curve had low sensitivity as can be seen in Figure 53 where the slope of the curve was 1.14 μA/ppm. This low sensitivity was caused by the CH_3COOH effect discussed in Section 4.3.2 and these data were collected before fully analyzing the pH study.

The low sensitivity resulted in a poor low detection limit, which was 10.5 ppm. The current limit for copper in drinking water, set by the EPA, is 1.3 ppm. From this it can be seen that the method needed to be improved.

To improve the sensitivity of the method, the knowledge gained from the pH study was applied and combined with the information from the amount of CNPs cast study to optimize the ΔI_{peak}. Solid $Cu(NO_3)_2$ was dissolved in a 1.0 M CH_3COONa solution to eliminate as mush of the CH_3COOH as possible. Also, the amount of CNPs cast was increased to 1.0 mg.

These changes had a significant effect on the sensitivity of the copper calibration curve. Figure 53 shows that the slope of the calibration curve, with the changes, was 13.8 μA/ppm. This was more than a tenfold increase and lowered the low detection limit to 0.5 ppm (500 ppb). This low detection limit was well below the limit set by the EPA.

Figures 53 and 54 show voltammograms associated with the two calibration curves. Because the system studied is not fully reversible, at low concentrations the $I_{reverse}$ peak nearly disappears resulting in a slight shift of the peak. This was well demonstrated in Figure 54. Also, a hump in the background around -3.7 V decreases with decreasing current, which demonstrates the need to use the second method of measuring peak current discussed in Section 4.1.1.

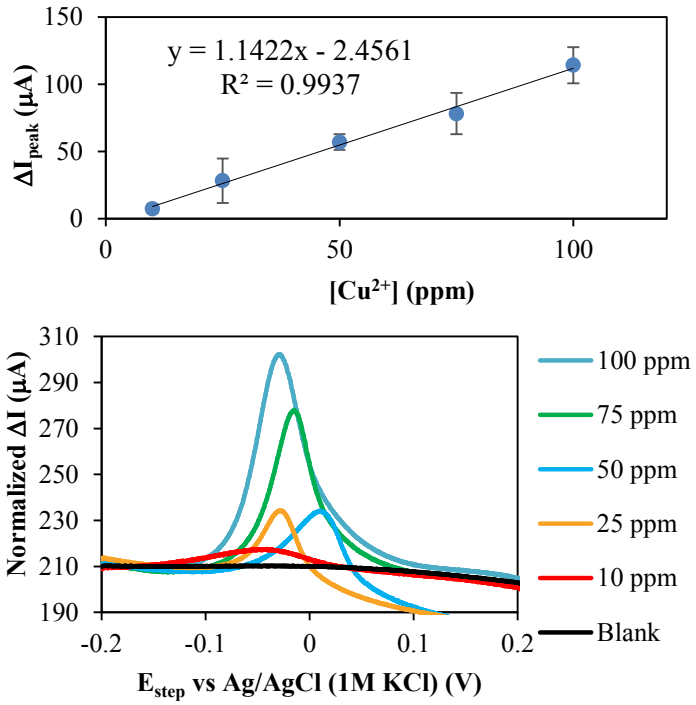

Figure 53: First Copper Calibration Curve. The copper calibration curve was obtained using analyte solutions made from a 1000 ppm Cu^{2+} in 2% HNO_3 and the 1.0 M CH_3COONa solution (top) and example voltammograms associated with the calibration curve (bottom). Error bars are at the 95% confidence level.

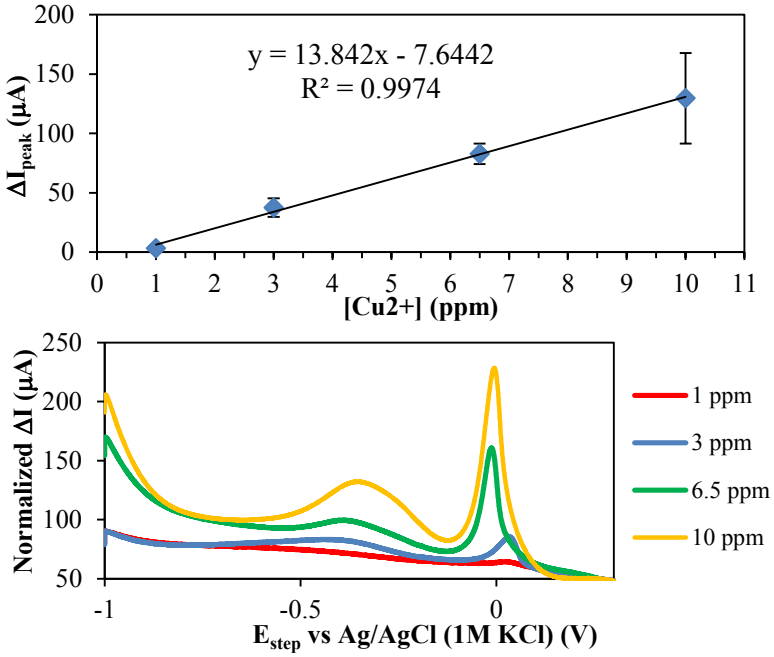

Figure 54: Final Copper Calibration Curve. The copper calibration curve was obtained using analyte solutions made from $Cu(NO_3)_2$ solid and the 1.0 M CH_3COONa solution (top) and example voltammograms associated with the calibration curve (bottom). Error bars are at the 95% confidence level.

4.4.0 SWV Detection of Mercury

This section will discuss the detection of mercury using the CNP-3 modified GCEs. The method was not optimized for mercury due to time constraints, so the following is the preliminary work on mercury detection. The work with mercury was performed between the two copper calibration curves and therefore the parameters used for the first copper calibration curve were used. These were: 0.5 mg of CNPs-3 cast and the analyte solutions had a pH of 6.0. The mercury analyte solutions were prepared from a 1000 ppm Hg^{2+} standard solution with 3% HNO_3. Due to the larger amount of HNO_3, more CH_3COONa needed to be added for adjustment of the pH to 6.0. Because of this, the CH_3COONa concentration was increased to 2.0 M. It was decided that keeping the pH the same was more important than the concentration of the CH_3COONa for

consistency in the procedure between metals and because at that time is was thought that pH was a controlling factor on the ΔI_{peak}.

The calibration curve for the detection of mercury is shown in Figure 55. The sensitivity of the curve was even lower than that of the first copper calibration curve at 0.99 μA/ppm. As before the low sensitivity and, in this case, the large variation between runs contributed to a low detection limit of 31 ppm. This low detection limit shows the need for further optimization for mercury detection. The large error bars are at the 95% confidence level and shows how large the variation between runs was.

Figure 55 shows example voltammograms used for the calibration curve. The peak for the mercury was around 0.15 V. There was some drift in the peak position at low concentrations similar to the copper voltammograms.

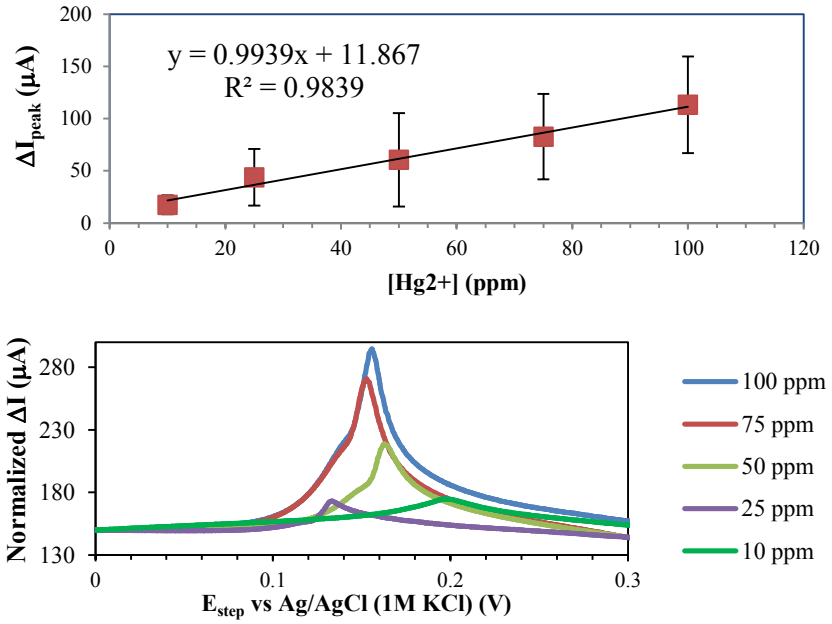

Figure 55: Mercury Calibration Curve. The mercury calibration curve was obtained using analyte solutions made from the Hg^{2+} in 3% HNO_3 solution and the 2.0 M CH_3COONa solution (top) and example voltammograms associated with the calibration curve (bottom). Error bars are at the 95% confidence level.

4.5.0 SWV Detection of Lead

The detection of lead with this system proved to be challenging. At first the procedure from the copper and mercury was carried over, but this resulted in a calibration curve that had a sensitivity lower than that of both copper and mercury. Then the system had to be optimized for lead. This process will be discussed in this section.

The first attempt at a calibration curve can be seen in Figure 56. As mentioned above, the slope of the curve was 0.37 mA/ppm, which shows the low sensitivity. Also, 100 ppm was the lowest concentration detectable. With the poor results of this attempt, a low detection limit analysis of the data was not performed.

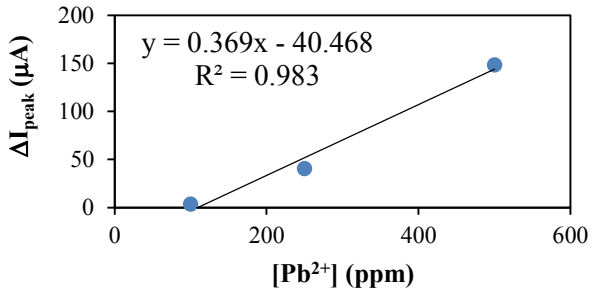

Figure 56: First Lead Calibration Curve. The lead calibration curve was obtained using analyte solutions made from a 1000 ppm Pb^{2+} in 2% HNO_3 and the 1.0 M CH_3COONa solution.

We decided to try a different electrolyte solution in the three electrode cell. The electrolyte chosen was a 1.0 M CH_3COONa solution and the pH of this solution was tested. Testing showed a large increase in the ΔI_{peak} observed, while the pH of the electrolyte solution made little difference (see Figure 57). These data points were collected from accumulation in a 50 ppm Pb^{2+} in 1.0 M CH_3COONa. You can compare the data from this graph to the 100 ppm point on the calibration curve above Notice that,

instead of a ΔI_{peak} of ~1 μA for 100 ppm (calibration curve above), the ΔI_{peak} for the 50 ppm was ~100 μA (with CH_3COONa as electrolyte). We chose to use pH 4.50 for continuing studies because the ΔI_{peak} can be considered to relatively unchanged from electrolyte pH 3.0-5.5. Also, pH 4.5 gave the largest ΔI_{peak}, but this could be within the error of the experiment, and it was in the middle of the range.

Changing the electrolyte had a significant impact on the calibration curve as well (see Figure 58). The slope of this calibration curve was 0.78 μA/ppm, double that of the first calibration curve. Also, concentrations as low as 10 ppm were detectable. This was 10 times less than the previous curve.

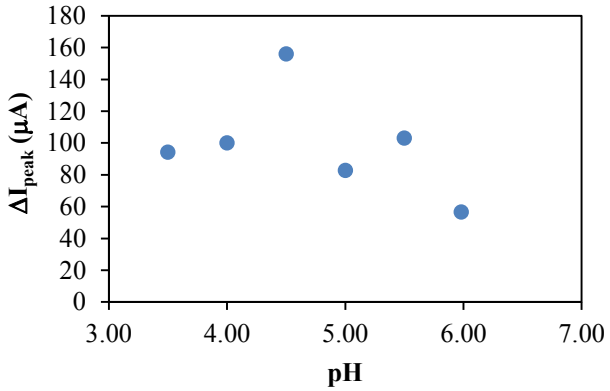

Figure 57: CH_3COONa Electrolyte pH Study. Data was obtained by accumulating CNP-3 modified GCEs in a 50 ppm Pb^{2+} in 1.0 M CH_3COONa analyte solution and performing SWV with 1.0 M CH_3COONa buffer as the electrolyte solution. The pH of the electrolyte solution was varied by adjustment with 1.0 M CH3COOH.

Next, the analyte solution was changed to test the effect of the CH_3COONa buffer on the voltammograms. To do this, the CH_3COONa was removed from the analyte solution by dissolving $Pb(NO_3)_2$ in deionized water. A 10 ppm Pb^{2+} solution was made, tested, and compared to the previous results. This increased the ΔI_{peak} by nearly 10 times

(see Figure 59). With these changes, it was decided that optimization of the amount of CNPs-3 cast on the GCEs should be performed, for the detection of lead, as well.

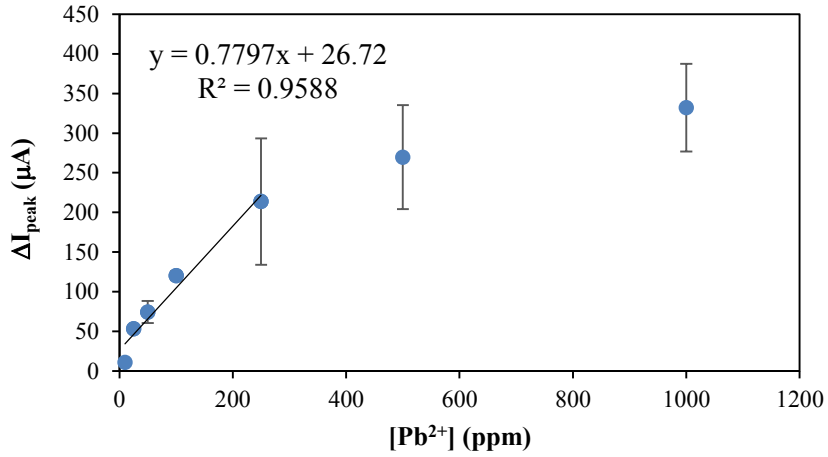

Figure 58: Second Lead Calibration Curve. The lead calibration curve was obtained using analyte solutions made from a 1000 ppm Pb^{2+} in 2% HNO_3 and the 1.0 M CH_3COONa solution. The electrolyte was 1.0 M CH_3COONa buffer (pH 4.50). Error bars are at the 95% confidence level.

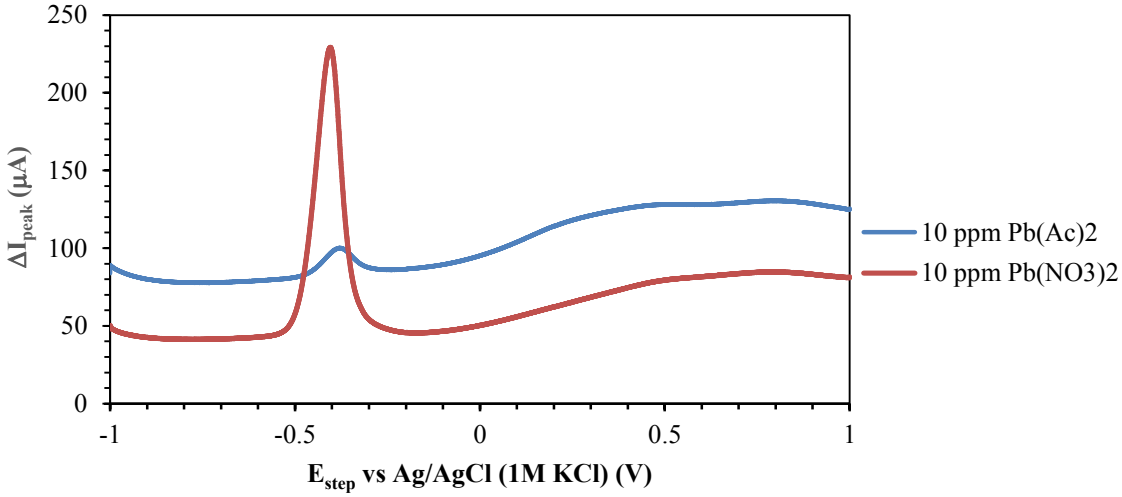

Figure 59: Voltammograms showing the Effect of CH_3COONa in the Analyte Solution on Peak Current for Lead Detection. SWV voltammograms of 10 ppm Pb^{2+} analyte solutions with and without 1.0 M CH_3COONa. The electrolyte solution was 1.0 M CH_3COONa buffer with pH of 4.50.

The amount of CNPs-3 cast on the GCE for lead detection study was performed with an analyte solution of 10 ppm Pb^{2+} without CH_3COONa. The heat treatment time was 1 min; the same as above. Figure 60 shows that the ΔI_{peak} increased up to 2.1 mg added and then decreased at 2.6 mg. Although 2.1 mg gave the largest amount of variation, it was chosen as the new casting amount, in order to maximize sensitivity.

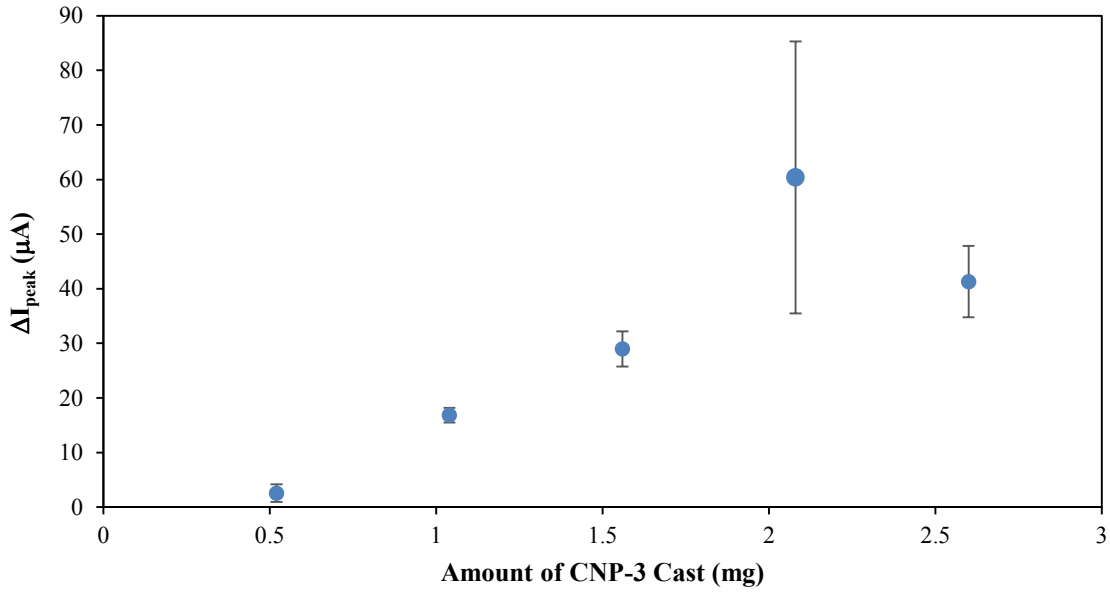

Figure 60: Optimization of CNP-3 Modified GCE Based on Amount of CNPs Cast for Lead Detection. The solution cast had a CNP-3 concentration of 26 mg/mL. The solution was cast in 10 μL increments and dried between each casting. The electrodes were accumulated in 10 ppm Pb^{2+} solution without CH_3COONa and the electrolyte was the 1.0 M CH_3COONa solution. Error bars are at the 95% confidence level.

The final calibration curve for the detection of lead was a significant improvement over the first attempt. From Figure 61 it can be seen that the slope of the curve was 40.4 μA/ppm. This was slightly more than a hundredfold increase in the sensitivity versus the first calibration curve attempt. The resulting low detection limit was 0.30 ppm (300 ppb).

Although this detection limit is higher than limit for drinking water, the progress made has been significant.

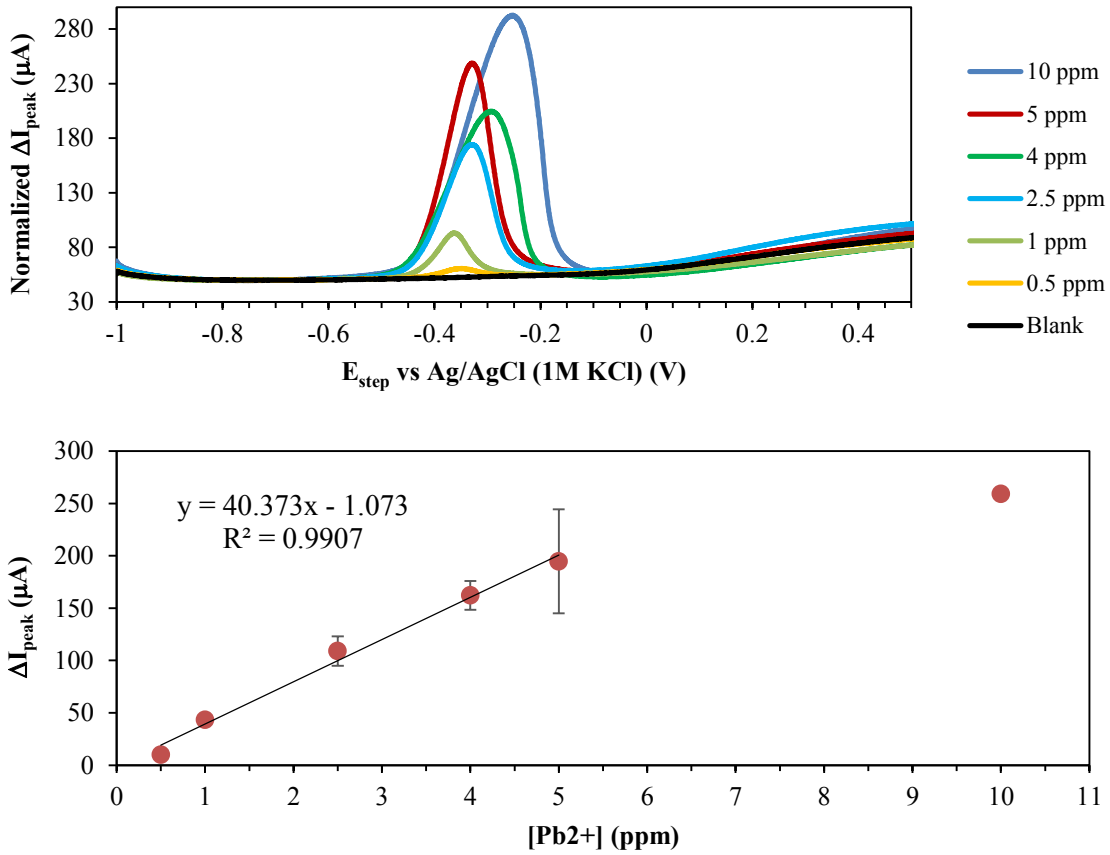

Figure 61: Final Lead Calibration Curve. Example voltammograms associated with the final lead calibration curve (top) and the final lead calibration curve (bottom). The electrodes were accumulated in Pb^{2+} solutions without CH_3COONa and the electrolyte was the 1.0 M CH_3COONa solution. Error bars are at the 95% confidence level.

An attempt was made to take everything learned from the lead calibration curves and apply them to copper and mercury calibration curves. The results showed no increase in the ΔI_{peak} for neither copper nor mercury. In fact no peak was observed for either. It seems that the presence of the CH_3COONa is important for detection of these two metals using the CNPs.

CHAPTER 5: CONCLUSIONS AND FUTURE WORK

5.1.0 Conclusions

The goal of this research was to fabricate fluorescent carbon nanoparticles and find an application for them. This goal was successfully accomplished. The journey to get to this point was a very long process. Along the way small improvements gave way to better results. In this Chapter the progress made on this project as well as some possible improvements and other future work will be covered.

5.1.1 CNP Synthesis. Glycerol had been used before to make CNPs, but never without another possible carbon source. These carbon sources were generally polymers. This previous work gave the inspiration to find a way to make CNPs without the presence of another carbon source. This process began by thermally decomposing glycerol in a household microwave, which yielded very little product, since the glycerol decomposed most effectively as a thin film on a hot surface. From this it was determined that a larger surface area was needed.

Silica gel was chosen as a means to increase the surface area. This was the first major breakthrough on this project. For the first time, CNPs were isolate as a dry powder. These CNPs-1 were highly fluorescent and water soluble.

Once the CNPs were able to be produced, it was decided that changes in the reaction conditions should be tested to see if that would change the properties of CNPs. In the literature H_3PO_4 had been used to create CNPs with a fluorescence peak that was shifted toward longer wavelengths.[2] Duplication of this was attempted and instead of a

shift in the fluorescence, CNPs-2 with an increased number of carboxylic acid functional groups were obtained.

The results obtained from adding in H_3PO_4 lead us to try to produce CNPs without silica gel and with only H_3PO_4. When this was attempted it was learned that CNPs could be made without the silica gel. This greatly reduced the amount of time needed to isolate the CNPs-3. The separation of CNPs from the silica gel took two to three days.

With the increase in carboxylic acid groups in CNPs-2 and CNPs-3, the water solubility was greatly reduced and pH dependent. This was fortuitous, because it allowed them to be used for the detection of heavy metals in aqueous solutions. Without the reduced solubility, the CNPs would simply dissolve off the electrode into the solution.

The increased number of carboxylic acid groups had another benefit: reduction in the workup and purification time. For the CNPs-1, the purification process employed dialysis, which takes quite a bit of time to perform. With the additional carboxylic acid groups the CNPs could be purified by extraction. The overall time to obtain dry CNPs went from approximately one week, for the CNPs-1, to a few days with CNPs-3.

5.1.2 Optical Properties. The optical properties of the CNPs were thoroughly studied. The absorbance spectra of the CNPs created from all three synthesis methods were very similar. They absorbed the greatest in the ultraviolet region and the absorbance trailed off toward zero at longer wavelengths.

The fluorescence spectrum was influenced by several factors. We showed that increasing concentration shifted the fluorescence peak toward longer wavelengths. A similar phenomenon was observed when the excitation wavelength was changed to

longer wavelengths. The pH of the solution containing the CNPs, affects the fluorescence peak as well. At high pH the fluorescence peak shifts toward shorter wavelengths and at low pH it shifts to longer wavelengths.

5.1.3 SWV Detection of Lead, Copper, and Mercury. The CNPs can be used to detect heavy metals. The low detection limits obtained for copper, lead, and mercury were 0.5, 0.3, and 10 ppm respectively. Copper had a detection limit lower than the MCL set by the EPA. Lead showed the best sensitivity at 40.4 μA/ppm, followed by copper at 13.8 μA/ppm, then mercury at 0.994 μA/ppm. Further, it was demonstrated that the sensitivity could be improved through experimentation and each metal must be optimized separately.

5.2.0 Future Work

There are many places where this research could go. Since these particles suspend well in in small chain, polar organic solvents, such as methanol or acetone, they could be printed by an ink jet printer to make electrodes for the detection of heavy metals. Also, there are many applications for their fluorescence as seen in the literature. These could be cell imaging, solar cells, or as a photothermal cell treatment.

With more work on the detection of heavy metals it may be possible to detect concentrations lower than those reported here. Detection of mercury was not optimized in this research, so the detection limit could easily be reduced with little effort. Different electrolyte solutions should be tested for each metal to further optimize the process and the same should be performed for the accumulation solutions as well.

Elucidation of the mechanism by which the CNPs are synthesized was beyond the scope of this research. It is well document in literature that glycerol thermally decomposes into acrolein and a few other products. We believe that this is the one of the early steps in the mechanism. To provide evidence for this, the reactions should be carried out with removal of samples at short time intervals at the beginning of the synthesis. These samples could be analyzed and structures of the intermediated might be determined. Knowing the structures of intermediates should provide evidence for the mechanism and even, possible internal and surface structures of the particles. Computational studies might complement such experimental attempts.

REFERENCES

1. Dekaliuk, M. O.; Viagin, O.; Malyukin, Y. V.; Demchenko, A. P., Fluorescent carbon nanomaterials: "quantum dots" or nanoclusters? *Physical Chemistry Chemical Physics* **2014,** *16* (30), 16075-16084.

2. Hola, K.; Bourlinos, A. B.; Kozak, O.; Berka, K.; Siskova, K. M.; Havrdova, M.; Tucek, J.; Safarova, K.; Otyepka, M.; Giannelis, E. P.; Zboril, R., Photoluminescence effects of graphitic core size and surface functional groups in carbon dots: COO− induced red-shift emission. *Carbon* **2014,** *70* (0), 279-286.

3. Xu, X.; Ray, R.; Gu, Y.; Ploehn, H. J.; Gearheart, L.; Raker, K.; Scrivens, W. A., Electrophoretic Analysis and Purification of Fluorescent Single-Walled Carbon Nanotube Fragments. *Journal of the American Chemical Society* **2004,** *126* (40), 12736-12737.

4. Hines, D. A.; Kamat, P. V., Recent Advances in Quantum Dot Surface Chemistry. *ACS Applied Materials & Interfaces* **2014,** *6* (5), 3041-3057.

5. Zuo, P.; Xiao, D.; Gao, M.; Peng, J.; Pan, R.; Xia, Y.; He, H., Single-step preparation of fluorescent carbon nanoparticles, and their application as a fluorometric probe for quercetin. *Microchim Acta* **2014,** *181* (11-12), 1309-1316.

6. Hu, Q.; Paau, M. C.; Zhang, Y.; Gong, X.; Zhang, L.; Lu, D.; Liu, Y.; Liu, Q.; Yao, J.; Choi, M. M. F., Green synthesis of fluorescent nitrogen/sulfur-doped carbon dots and investigation of their properties by HPLC coupled with mass spectrometry. *RSC Advances* **2014,** *4* (35), 18065-18073.

7. Wei, X.-M.; Xu, Y.; Li, Y.-H.; Yin, X.-B.; He, X.-W., Ultrafast synthesis of nitrogen-doped carbon dots via neutralization heat for bioimaging and sensing applications. *RSC Advances* **2014,** *4* (84), 44504-44508.

8. Zhang, W.; Dai, D.; Chen, X.; Guo, X.; Fan, J., Red shift in the photoluminescence of colloidal carbon quantum dots induced by photon reabsorption. *Applied Physics Letters* **2014,** *104* (9), -.

9. Cui, Y.; Hu, Z.; Zhang, C.; Liu, X., Simultaneously enhancing up-conversion fluorescence and red-shifting down-conversion luminescence of carbon dots by a simple hydrothermal process. *Journal of Materials Chemistry B* **2014,** *2* (40), 6947-6952.

10. Tu, X.; Ma, Y.; Cao, Y.; Huang, J.; Zhang, M.; Zhang, Z., PEGylated carbon nanoparticles for efficient in vitro photothermal cancer therapy. *Journal of Materials Chemistry B* **2014,** *2* (15), 2184-2192.

11. Gong, J.; An, X.; Yan, X., A novel rapid and green synthesis of highly luminescent carbon dots with good biocompatibility for cell imaging. *New Journal of Chemistry* **2014,** *38* (4), 1376-1379.

12. Wang, W.; Lu, Y.-C.; Huang, H.; Feng, J.-J.; Chen, J.-R.; Wang, A.-J., Facile synthesis of water-soluble and biocompatible fluorescent nitrogen-doped carbon dots for cell imaging. *Analyst* **2014,** *139* (7), 1692-1696.

13. Luo, P. G.; Yang, F.; Yang, S.-T.; Sonkar, S. K.; Yang, L.; Broglie, J. J.; Liu, Y.; Sun, Y.-P., Carbon-based quantum dots for fluorescence imaging of cells and tissues. *RSC Advances* **2014,** *4* (21), 10791-10807.

14. Lu, Y.; Zhang, L.; Lin, H., The Use of a Microreactor for Rapid Screening of the Reaction Conditions and Investigation of the Photoluminescence Mechanism of Carbon Dots. *Chemistry – A European Journal* **2014,** *20* (15), 4246-4250.

15. Xu, Y.; Li, Y.-H.; Wang, Y.; Cui, J.-L.; Yin, X.-B.; He, X.-W.; Zhang, Y.-K., 13C-engineered carbon quantum dots for in vivo magnetic resonance and fluorescence dual-response. *Analyst* **2014,** *139* (20), 5134-5139.

16. Xu, Y.; Liu, J.; Gao, C.; Wang, E., Applications of carbon quantum dots in electrochemiluminescence: A mini review. *Electrochemistry Communications* **2014,** *48* (0), 151-154.

17. Khene, S.; Nyokong, T., Characterization of Quantum Dots, Single Walled Carbon Nanotubes and Nickel Octadecyphthalocyanine Conjugates. *International Journal of Nanoscience* **2012,** *11* (02), 1250022.

18. Mao, L.-H.; Tang, W.-Q.; Deng, Z.-Y.; Liu, S.-S.; Wang, C.-F.; Chen, S., Facile Access to White Fluorescent Carbon Dots toward Light-Emitting Devices. *Industrial & Engineering Chemistry Research* **2014**.

19. Narayanan, R.; Deepa, M.; Srivastava, A. K., Forster resonance energy transfer and carbon dots enhance light harvesting in a solid-state quantum dot solar cell. *Journal of Materials Chemistry A* **2013,** *1* (12), 3907-3918.

20. Chen, L.; Guo, C. X.; Zhang, Q.; Lei, Y.; Xie, J.; Ee, S.; Guai, G.; Song, Q.; Li, C. M., Graphene Quantum-Dot-Doped Polypyrrole Counter Electrode for High-Performance Dye-Sensitized Solar Cells. *ACS Applied Materials & Interfaces* **2013,** *5* (6), 2047-2052.

21. Huang, P.; Lin, J.; Wang, X.; Wang, Z.; Zhang, C.; He, M.; Wang, K.; Chen, F.; Li, Z.; Shen, G.; Cui, D.; Chen, X., Light-Triggered Theranostics Based on Photosensitizer-Conjugated Carbon Dots for Simultaneous Enhanced-Fluorescence Imaging and Photodynamic Therapy. *Advanced Materials* **2012,** *24* (37), 5104-5110.

22. Xie, S.; Su, H.; Wei, W.; Li, M.; Tong, Y.; Mao, Z., Remarkable photoelectrochemical performance of carbon dots sensitized TiO2 under visible light irradiation. *Journal of Materials Chemistry A* **2014,** *2* (39), 16365-16368.

23. Luo, P.; Li, C.; Shi, G., Synthesis of gold@carbon dots composite nanoparticles for surface enhanced Raman scattering. *Physical Chemistry Chemical Physics* **2012,** *14* (20), 7360-7366.

24. Wang, C.; Wu, X.; Li, X.; Wang, W.; Wang, L.; Gu, M.; Li, Q., Upconversion fluorescent carbon nanodots enriched with nitrogen for light harvesting. *Journal of Materials Chemistry* **2012,** *22* (31), 15522-15525.

25. Wang, F.; Xie, Z.; Liu, C.-y., Mechanically strong and highly luminescent macroporous monolith by crosslinking of carbon nanodots. *New Journal of Chemistry* **2014,** *38* (4), 1601-1605.

26. Lin, Z.; Xue, W.; Chen, H.; Lin, J.-M., Classical oxidant induced chemiluminescence of fluorescent carbon dots. *Chemical Communications* **2012,** *48* (7), 1051-1053.

27. Cayuela, A.; Laura Soriano, M.; Valcárcel, M., Strong luminescence of Carbon Dots induced by acetone passivation: Efficient sensor for a rapid analysis of two different pollutants. *Analytica Chimica Acta* **2013,** *804* (0), 246-251.

28. Cayuela, A.; Soriano, M. L.; Carrión, M. C.; Valcárcel, M., Functionalized carbon dots as sensors for gold nanoparticles in spiked samples: Formation of nanohybrids. *Analytica Chimica Acta* (0).

29. Gaddam, R. R.; D, V.; Narayan, R.; Raju, K. V. S. N., Controllable synthesis of biosourced blue-green fluorescent carbon dots from camphor for the detection of heavy metal ions in water. *RSC Advances* **2014**.

30. Hu, S.; Zhao, Q.; Dong, Y.; Yang, J.; Liu, J.; Chang, Q., Carbon-Dot-Loaded Alginate Gels as Recoverable Probes: Fabrication and Mechanism of Fluorescent Detection. *Langmuir* **2013,** *29* (40), 12615-12621.

31. Li, J.; Wang, N.; Tran.T, T.; Huang, C. a.; Chen, L.; Yuan, L.; Zhou, L.; Shen, R.; Cai, Q., Electrogenerated chemiluminescence detection of trace level pentachlorophenol using carbon quantum dots. *Analyst* **2013,** *138* (7), 2038-2043.

32. Xu, J.; Sahu, S.; Cao, L.; Bunker, C. E.; Peng, G.; Liu, Y.; Fernando, K. A. S.; Wang, P.; Guliants, E. A.; Meziani, M. J.; Qian, H.; Sun, Y.-P., Efficient Fluorescence Quenching in Carbon Dots by Surface-Doped Metals - Disruption of Excited State Redox Processes and Mechanistic Implications. *Langmuir* **2012,** *28* (46), 16141-16147.

33. Luo, P. G.; Sahu, S.; Yang, S.-T.; Sonkar, S. K.; Wang, J.; Wang, H.; LeCroy, G. E.; Cao, L.; Sun, Y.-P., Carbon "quantum" dots for optical bioimaging. *Journal of Materials Chemistry B* **2013,** *1* (16), 2116-2127.

34. Lai, C.-W.; Hsiao, Y.-H.; Peng, Y.-K.; Chou, P.-T., Facile synthesis of highly emissive carbon dots from pyrolysis of glycerol; gram scale production of carbon

dots/mSiO2 for cell imaging and drug release. *Journal of Materials Chemistry* **2012,** *22* (29), 14403-14409.

35. Shi, Q.-Q.; Li, Y.-H.; Xu, Y.; Wang, Y.; Yin, X.-B.; He, X.-W.; Zhang, Y.-K., High-yield and high-solubility nitrogen-doped carbon dots: formation, fluorescence mechanism and imaging application. *RSC Advances* **2014,** *4* (4), 1563-1566.

36. Liu, C.; Zhang, P.; Zhai, X.; Tian, F.; Li, W.; Yang, J.; Liu, Y.; Wang, H.; Wang, W.; Liu, W., Nano-carrier for gene delivery and bioimaging based on carbon dots with PEI-passivation enhanced fluorescence. *Biomaterials* **2012,** *33* (13), 3604-3613.

37. Liu, C.; Zhang, P.; Tian, F.; Li, W.; Li, F.; Liu, W., One-step synthesis of surface passivated carbon nanodots by microwave assisted pyrolysis for enhanced multicolor photoluminescence and bioimaging. *Journal of Materials Chemistry* **2011,** *21* (35), 13163-13167.

38. Wei, J.; Zhang, X.; Sheng, Y.; Shen, J.; Huang, P.; Guo, S.; Pan, J.; Liu, B.; Feng, B., Simple one-step synthesis of water-soluble fluorescent carbon dots from waste paper. *New Journal of Chemistry* **2014,** *38* (3), 906-909.

39. Fu, C.; Qiang, L.; Liu, T.; Tan, L.; Shi, H.; Chen, X.; Ren, X.; Meng, X., Ultrafast chemical aerosol flow synthesis of biocompatible fluorescent carbon dots for bioimaging. *Journal of Materials Chemistry B* **2014,** *2* (40), 6978-6983.

40. Zhang, Z.; Shi, Y.; Pan, Y.; Cheng, X.; Zhang, L.; Chen, J.; Li, M.-J.; Yi, C., Quinoline derivative-functionalized carbon dots as a fluorescent nanosensor for sensing and intracellular imaging of Zn2+. *Journal of Materials Chemistry B* **2014,** *2* (31), 5020-5027.

41. Lee, C. H.; Rajendran, R.; Jeong, M.-S.; Ko, H. Y.; Joo, J. Y.; Cho, S.; Chang, Y. W.; Kim, S., Bioimaging of targeting cancers using aptamer-conjugated carbon nanodots. *Chemical Communications* **2013,** *49* (58), 6543-6545.

42. Masiakowski, P.; Breathnach, R.; Bloch, J.; Gannon, F.; Krust, A.; Chambon, P., Cloning of cDNA sequences of hormone-regulated genes from the MCF-7 human breast cancer cell line. *Nucleic Acids Research* **1982,** *10* (24), 7895-7903.

43. Barman, S.; Sadhukhan, M., Facile bulk production of highly blue fluorescent graphitic carbon nitride quantum dots and their application as highly selective and sensitive sensors for the detection of mercuric and iodide ions in aqueous media. *Journal of Materials Chemistry* **2012,** *22* (41), 21832-21837.

44. Zhai, Y.; Zhu, Z.; Zhu, C.; Ren, J.; Wang, E.; Dong, S., Multifunctional water-soluble luminescent carbon dots for imaging and Hg2+ sensing. *Journal of Materials Chemistry B* **2014,** *2* (40), 6995-6999.

45. Wang, Q.; Liu, X.; Zhang, L.; Lv, Y., Microwave-assisted synthesis of carbon nanodots through an eggshell membrane and their fluorescent application. *Analyst* **2012,** *137* (22), 5392-5397.

46. Shinde, D. B.; Pillai, V. K., Electrochemical Preparation of Luminescent Graphene Quantum Dots from Multiwalled Carbon Nanotubes. *Chemistry – A European Journal* **2012,** *18* (39), 12522-12528.

47. Niu, J.; Gao, H.; Wang, L.; Xin, S.; Zhang, G.; Wang, Q.; Guo, L.; Liu, W.; Gao, X.; Wang, Y., Facile synthesis and optical properties of nitrogen-doped carbon dots. *New Journal of Chemistry* **2014,** *38* (4), 1522-1527.

48. Su, Y.; Xie, M.; Lu, X.; Wei, H.; Geng, H.; Yang, Z.; Zhang, Y., Facile synthesis and photoelectric properties of carbon dots with upconversion fluorescence using arc-synthesized carbon by-products. *RSC Advances* **2014,** *4* (10), 4839-4842.

49. Kwon, W.; Do, S.; Rhee, S.-W., Formation of highly luminescent nearly monodisperse carbon quantum dots via emulsion-templated carbonization of carbohydrates. *RSC Advances* **2012,** *2* (30), 11223-11226.

50. Philippidis, A.; Spyros, A.; Anglos, D.; Bourlinos, A.; Zbořil, R.; Giannelis, E., Carbon-dot organic surface modifier analysis by solution-state NMR spectroscopy. *J Nanopart Res* **2013,** *15* (7), 1-9.

51. Yin, J.-Y.; Liu, H.-J.; Jiang, S.; Chen, Y.; Yao, Y., Hyperbranched Polymer Functionalized Carbon Dots with Multistimuli-Responsive Property. *ACS Macro Letters* **2013,** *2* (11), 1033-1037.

52. Anilkumar, P.; Wang, X.; Cao, L.; Sahu, S.; Liu, J.-H.; Wang, P.; Korch, K.; Tackett Ii, K. N.; Parenzan, A.; Sun, Y.-P., Toward quantitatively fluorescent carbon-based "quantum" dots. *Nanoscale* **2011,** *3* (5), 2023-2027.

53. Sun, Y.-P.; Zhou, B.; Lin, Y.; Wang, W.; Fernando, K. A. S.; Pathak, P.; Meziani, M. J.; Harruff, B. A.; Wang, X.; Wang, H.; Luo, P. G.; Yang, H.; Kose, M. E.; Chen, B.; Veca, L. M.; Xie, S.-Y., Quantum-Sized Carbon Dots for Bright and Colorful Photoluminescence. *Journal of the American Chemical Society* **2006,** *128* (24), 7756-7757.

54. Hu, C.; Yu, C.; Li, M.; Wang, X.; Yang, J.; Zhao, Z.; Eychmüller, A.; Sun, Y. P.; Qiu, J., Chemically Tailoring Coal to Fluorescent Carbon Dots with Tuned Size and Their Capacity for Cu(II) Detection. *Small* **2014**, n/a-n/a.

55. Li, Y.; Zhong, X.; Rider, A. E.; Furman, S. A.; Ostrikov, K., Fast, energy-efficient synthesis of luminescent carbon quantum dots. *Green Chemistry* **2014,** *16* (5), 2566-2570.

56. Morton, J.; Havens, N.; Mugweru, A.; Wanekaya, A. K., Detection of Trace Heavy Metal Ions Using Carbon Nanotube- Modified Electrodes. *Electroanalysis* **2009,** *21* (14), 1597-1603.

57. Agency, U. S. E. P. Drinking Water Contaminants Page. http://water.epa.gov/drink/contaminants/index.cfm#one (accessed September 1, 2015).

58. Atkins, P. W.; De Paula, J.; Friedman, R., *Quanta, matter, and change : a molecular approach to physical chemistry*. Oxford University Press: Oxford ; New York, 2009; p xxi, 782 p.

59. Skoog, D. A.; Holler, F. J.; Crouch, S. R., *Principles of instrumental analysis*. 6th ed.; Thomson Brooks/Cole: Belmont, CA, 2007; p xv, 1039 p.

60. Hou, J.; Dong, J.; Zhu, H.; Teng, X.; Ai, S.; Mang, M., A simple and sensitive fluorescent sensor for methyl parathion based on l-tyrosine methyl ester functionalized carbon dots. *Biosensors and Bioelectronics* **2015,** *68*, 20-26.

61. Harris, D. C., *Quantitative chemical analysis*. 7th ed.; W.H. Freeman and Co.: New York, NY, 2007.